

Accepted Manuscript

Petroleum Geoscience

Investigating the PS seismic imaging of faults using seismic modelling and data from the Snøhvit field, Barents Sea

Jennifer Cunningham, Wiktor W. Weibull, Nestor Cardozo & David Iacopini

DOI: <https://doi.org/10.1144/petgeo2020-044>

To access the most recent version of this article, please click the DOI URL in the line above. When citing this article please include the above DOI.

Received 10 April 2020

Revised 14 November 2021

Accepted 29 November 2021

© 2021 The Author(s). Published by The Geological Society of London for GSL and EAGE. All rights reserved. For permissions: <http://www.geolsoc.org.uk/permissions>. Publishing disclaimer: www.geolsoc.org.uk/pub_ethics

Supplementary material at <https://doi.org/10.6084/m9.figshare.c.5727552>

Manuscript version: Accepted Manuscript

This is a PDF of an unedited manuscript that has been accepted for publication. The manuscript will undergo copyediting, typesetting and correction before it is published in its final form. Please note that during the production process errors may be discovered which could affect the content, and all legal disclaimers that apply to the journal pertain.

Although reasonable efforts have been made to obtain all necessary permissions from third parties to include their copyrighted content within this article, their full citation and copyright line may not be present in this Accepted Manuscript version. Before using any content from this article, please refer to the Version of Record once published for full citation and copyright details, as permissions may be required.

Investigating the PS seismic imaging of faults using seismic modelling and data from the Snøhvit field, Barents Sea

Jennifer Cunningham^{*1}, Wiktor W. Weibull¹, Nestor Cardozo¹, David Iacopini²

¹Department of Energy Resources, University of Stavanger, 4036 Stavanger, Norway

+47 461 84 478*, JCUNN@equinor.com

²DISTAR, Università degli Studi di Napoli Federico II

Keywords:

Fault imaging, PS data, seismic modelling, azimuthal separation, incidence angle, frequency

Abstract:

PS seismic data from the Snøhvit field are compared with seismic modelling to understand the effect of azimuthal separation and incidence angle on the imaging of faults and associated horizon discontinuities. In addition, the frequency content of seismic waves backscattered from faults is analysed. The study area consists of a horst structure delimited by a northern fault dipping NW and oblique to the E-W survey orientation, and a southern fault dipping SSW and subparallel to the survey. Due to the raypath asymmetry of PS reflections, the northern fault is imaged better by azimuthally partitioned W data that include receivers downdip of the fault, relative to the sources, than by E data where the receivers are updip from the sources. Partial stack data show a systematic increase in the PS fault-reflected amplitude and therefore quality of fault imaging with increasing incidence angle. Fault images are dominated by internal low-medium frequency shadows surrounded by medium-high frequencies haloes. Synthetic experiments suggest that this is due to the interaction of specular waves and diffractions, and the spectral contribution from the fault signal, which increases with fault zone complexity. These results highlight the impact of survey geometry and processing workflows on fault imaging.

1. Introduction:

The analysis of faults in seismic data has been an important topic in the petroleum industry for decades due to the role of faults as critical elements in many oil and gas fields, in waste (CO₂) or energy storage, and in geothermal energy. Fault analysis in seismic data has evolved from simple interpretation on cross sections or time/depth slices, to detailed interpretation using a range of structure-enhancing attributes (e.g. Iacopini & Butler 2011; Iacopini *et al.* 2012, 2016; Torabi *et al.* 2017). High resolution seismic imaging of faults in 3D is essential for the understanding of fault geometry, displacement profiles, fault juxtaposition and sealing, and fault formation through interaction and linkage (Dawers & Underhill 2000; Elliott *et al.* 2012; Long & Imber 2012; Tvedt *et al.* 2013; Osagiede *et al.* 2014). Despite this, few studies focus on understanding how faults are imaged with respect to both real and modelled data. Fault imaging is referred to in two different contexts in this study: fault plane imaging which is the imaging of the fault as a distinct reflector, and discontinuity imaging which is the identification of displaced seismic reflectors but without the imaging of the fault itself.

When P-waves (primary wave, compressional wave) penetrate the subsurface and reflect off a boundary, they can reflect as either a P-wave (PP reflection) or an S-wave (PS reflection). PP seismic data are by far the most common type of subsurface data used in fault interpretation, since they are the most common type of data collected by conventional towed-streamer marine seismic surveys. Improvements in seismic acquisition and processing technology have enhanced the imaging of faults on PP data alone. However, onshore surveys and, since S-waves cannot travel through fluids, offshore surveys using arrays of ocean-bottom nodes placed directly on the ocean floor can also record S-waves. Ocean bottom seismic (OBS) data have been applied to illuminate structures (faults) below shallow gas, remove water-bottom or free-surface multiples, and determine hydrocarbon fluid distributions (Ensley 1984; Granli *et al.* 1999; Stewart *et al.* 2003; Xu & Tsvankin 2007; Farfour & Yoon 2016).

Seismic processing of PP and PS data from OBS surveys typically analyses the reflection signal as a function of incidence/reflection angle by generating incidence angle/offset stacks (i.e. near, mid and far offsets). Processing workflows can also be applied to separate data from a chosen source-receiver azimuth using specialized 4-component (4C) cable node technology (e.g. Stewart *et al.* 2002, 2003). Directionally (azimuthally) separated seismic data have been used in both carbonate and clastic systems to determine fracture orientations by analysing differences between the amplitude versus offset (AVO) responses parallel and perpendicular to fluid-filled fracture networks (azimuthal AVO; e.g. Jenner 2002; Perez & Marfurt 2007; Gray 2008). The logical extension of this work is to apply similar techniques to faults, and to our knowledge, azimuthal data filtering has not yet been applied to fault imaging.

Forward seismic modelling reveals a direct correlation between seismic amplitude variations and the amount of fault-related deformation (Botter *et al.* 2014, 2016, 2017a, b). Furthermore, higher frequencies in the synthetic seismic source resulted in higher resolution amplitude extractions from within the modelled fault zone (Botter *et al.* 2014). We observe that the quality of fault imaging with mode-converted PS data varies quite strongly with azimuthal illumination, and in this study, we investigate this observation by analysing both real data and synthetic data from simplified fault models.

The case study is on the western margin of the Snøhvit field, Norwegian Barents Sea. Pre-stack depth-migrated PS data from the field are used to study the effects of illumination on

the imaging of faults, and to evaluate the seismic frequency contained in and around faults. We find that fault imaging: (i) is significantly affected by azimuthal separation of the data, (ii) improves with increasing incidence angle, and (iii) can influence the frequency content of adjacent reflectors. Two forward seismic modelling experiments were designed to explain these observations: Experiment 1 (planar fault) explains the first and second observations, while experiment 2 (fault zone) illustrates the third observation.

2. The Snøhvit field: A case study

2.1 Geological setting

The Snøhvit gas and condensate field is in the centre of the Hammerfest Basin, southwest Barents Sea, and consists of an up-thrown fault block bounded by E-W trending faults within the overall NE-SW trending faults that define the Hammerfest Basin (Fig. 1a, b). Key reservoir intervals in the field are Lower-Middle Jurassic sandstones of the Tubåen, Nordmela and Stø formations (fms) (Fig. 1e). Jurassic-Cretaceous marine shales of the Fuglen, Hekkingen, Knurr and Kolje fms are principal sealing intervals (Linjordet & Olsen 1992). The Upper Triassic-Lower Cretaceous units have undergone extensional faulting and are the focus of this study (Fig. 1e).

Shallow gas is common in the Barents Sea and causes dimming and reduction in quality in the seismic imaging of the reservoir intervals due to deterioration of the PP seismic signal (Ostanin *et al.* 2012; Mohammedyasin *et al.* 2016). Since Snøhvit also has a shallow gas cloud affecting PP imaging, this study will focus on the PS data. A 5x5 km study area on the western margin of the field was chosen for this investigation because of the presence of faults oriented both parallel to, and oblique to the shooting orientation of the seismic survey (Fig. 1a-c). The study area consists of an up-thrown fault block defined by a northern fault that trends NE-SW, dips $\sim 54^\circ$ NW and is oblique to the E-W survey orientation (Fig. 1b-d, blue fault), and a southern fault that trends WNW-ESE, dips 50° SSW and is subparallel to the survey orientation (Fig. 1b-d, green fault).

2.2 An introduction to OBS data, seismic acquisition, and processing of the case study

Modern offshore seismic surveys begin by generating pressure waves (P-waves) using a man-made acoustic source (i.e. air-gun); the waves then reflect off boundaries between layers with different acoustic impedance as P or converted S-waves (Fig. 2, e.g. Garotta & Granger 1988; Landrø & Amundsen 2010). P-waves can travel through both solids and liquids and can therefore be recorded both onshore and in conventional marine acquisition. PP-surveys are the simplest, cheapest, and therefore most readily used seismic surveys. S-waves cannot travel through fluids and therefore can only be collected by geophones on land or by receiver nodes on the ocean floor. Since they cannot travel through fluids, S-waves are mainly sensitive to changes in lithology (though S-wave velocities are affected by changes in the density of fluids in the pore space). Marine surveys that collect S-wave data may be referred to as ocean bottom seismic or ocean bottom cable/node surveys (OBS, OBC or OBN; Barr 1997). Multiple P to S-wave conversions result in degradation of the seismic signal and the loss of high frequencies with depth (Stewart & Lawton 1996). Because converted-waves reflect asymmetrically about the normal to the reflector (Fig. 2), PS data can be more challenging to process than PP data (Stewart *et al.* 2002).

Four-component (4C) node technology is used in modern surveys to collect P and S-wave data in the form of particle velocity in three Cartesian directions (X, Y, Z) and pressure (e.g. Stewart *et al.* 2002, 2003). These nodes and swath acquisition design allow for the collection

of high-fold data and larger offset ranges than a standard towed-streamer marine survey (Landrø & Amundsen 2018). During processing, it is possible to filter the data by azimuth (i.e., the orientation of the receivers relative to the source) and by incidence angle (i.e., near, mid, far, and full stacks).

This study uses the ST15M01 ocean-bottom seismic (OBS) survey that was collected by Magseis AS in 2013 and processed by CGG in 2015 on behalf of the Snøhvit license partners in 2013. The nodes and seismic vessel swaths were oriented E-W (90-270°) to optimize the imaging beneath an E-W trending shallow gas cloud on the western flank of the Snøhvit Field (Fig. 1b, c). The typical crossline offset (N-S) varied between 600 m and 1175 m depending on the area, while the maximum inline offset (E-W) was around 10 km. As stated before, this study focuses only on the PS data.

In seismic pre-processing (Table 1), all azimuthally unseparated data went through the same set of processes (Table 1, Stages 1-23) before they were separated into east (E, only containing data from receivers positioned to the east of the source) and west (W, only containing data from receivers positioned to the west of the source) azimuths. The azimuthally separated data were migrated using a Kirchhoff pre-stack depth migration (PSDM) method. Once separated and migrated, the data were stretched to PS time and further converted into incidence angle stacks, where partial (near 10-25°, mid 20-45°, far 35-60°) and full-stack volumes were defined (Table 1, post-migration processing). A post-stack processing workflow was then applied (Table 1). All depths are referred to in two-way PS travel time (TWT) in milliseconds. In total, eight volumes (near, mid, far and full stack for both E and W azimuths) were used in this study, and for each volume a downwards increase in acoustic impedance is represented by a red seismic peak, and a decrease is represented by a blue trough.

3. Methods

This study involves a comparison and analysis of faults using a case study (3.1) and forward seismic modelling (3.2).

3.1 The seismic analysis of faults in the Snøhvit field

3.1.1 Fault imaging, incidence angle and azimuth

The aim of this part was to compare the quality of fault discontinuity imaging on different incidence angle stacks and azimuthally separated seismic volumes (E versus W), for the two faults of different orientation. Two methods were applied to address this question.

The first method examines reflection seismic and two volume attributes on the partial and full-stack seismic data volumes of the E and W azimuths. Tensor (Bakker, 2002) was the first attribute chosen because of its previous successful application to the analysis of faults (i.e. Botter *et al.* 2016; Iacopini *et al.* 2016; Cunningham *et al.* 2019), and because in this dataset it gives the clearest indication of fault imaging. Tensor is sensitive to both seismic amplitude changes and reflector continuity, and in the case of a fault displacing a horizon, it will show higher values at the discontinuity than in unfaulted areas. The tensor attribute was optimized for the studied faults, using a fault width and height of 7 and 21 voxels (87.5 m and 84 ms) respectively. In the horizontal, a voxel is equivalent to the inline and crossline spacing of the data which in this case was 12.5 m (7 x 12.5 = 87.5 m), while in the vertical, a voxel refers to the time sampling interval which in this case was 4 ms (4 x 21 = 84 ms). The second attribute chosen is envelope (Chopra & Marfurt 2007). This attribute was generated to visualize

changes in amplitude with increasing incidence angle across partial and full stack volumes. The original reflection data were also compared, and all data were displayed as a single crossline slice through the centre of the study area (Fig. 1c), and a time slice at 3128 ms (PS time), which is approximately at the middle of the faulted stratigraphic interval.

The second method blends the tensor responses of the near, mid and far angle stacks for both the E and W azimuths. Colour blending makes it possible to compare the relative contribution of signal from each of the partial stacks. This type of blend is termed an AVO colour blend (Gomez 2015). The blend comprises three equally scaled tensor volumes representing the near (red), mid (green) and far (blue) data. When a single colour (red, green or blue) is visible in the colour blend, it means that a single volume has the highest relative response. If magenta, yellow or cyan are visible, it means that two volumes have a similar relative response. White is representative of a high response from all three volumes, while black represents very little or no response. As in the first method, the results are displayed on a single time slice at 3128 ms.

3.1.2 The seismic frequency of faults

Frequency decomposition (FD) of the E and W partial and full-stack data were performed using the Exponential Constant Q method (ECQ; Jilinski and Wooltorton, 2016) in the Geoteric seismic analysis package. The frequency decompositions were generated by extracting a single power spectrum from the 3128 ms time slice of each of the seismic volumes. A short-window Fourier transform centred along the target time slice was used to calculate the power spectra for each trace. The individual trace spectra were then averaged to provide the power spectrum along the time slice (pers. comm., Geoteric, 2021). Using this power spectrum as a guide, constant Q decomposition bands with low, medium and high central frequencies were chosen (Jilinski & Wooltorton 2016). For the E and W near, mid, far and full-stack volumes, central frequencies of 8, 14 and 30 Hz were selected as they best fit the peaks in the power spectrum for each dataset. Magnitude volumes were generated for each of the central frequencies, and RGB colour blends were then generated by assigning red, green, and blue to the equally scaled 8, 14 and 30 Hz volumes, respectively. The reading of the colour in these blends is like the AVO colour blends (3.1.1). The frequency decomposition blends were displayed as a single inline, crossline and time slice at 3128 ms.

More detailed information on this method can be found in both Jilinski & Wooltorton (2016) and Han (2017). This frequency-decomposition method was chosen as it best honours the bandwidth of the seismic data at 3128 ms (PS time). Choosing a method that could be optimized for a single time slice was critical for the analysis of the faults in the Snøhvit data.

3.2 Forward seismic modelling

Two synthetic 2D seismic models were designed to study the effect of azimuthal separation, incidence angle stacking (experiment 1), and frequency content (experiment 2) on the imaging of faults. The forward-modelled seismic are representations of a simplified geological model, with the aim to highlight potential causes for the observed imaging anomalies in the Snøhvit field. The models are not a duplication of the Snøhvit data, but a heuristic approach to explain the observations made in the real seismic data.

3.2.1 Experiment 1

The first synthetic experiment is designed to model the effects of azimuthal separation and incidence-angle stacking on the seismic imaging of faults. The synthetic data in 2D were

generated using a finite-difference solution to the elastic wave equation (Virieux 1986), and a 14 km long, relatively simple, layered isotropic elastic model (Figs 3, 4a). Although anisotropy can significantly affect the imaging of faults, its impact on azimuthally opposed data should be similar and so we have chosen to omit this from the analysis. A single geological layer with a uniform thickness of 300 m was placed at approximately 2500 m depth, and it was displaced 150 m vertically by a discontinuity dipping 55° to the west (left of the image). No fault body was defined in the model. This method was chosen because from our observations, the fault planes are not directly imaged in the Snøhvit data. The lack of a fault body allowed us to focus on how reflections from a horizontal boundary can be influenced by the presence of a fault. Although in the models the discontinuity appears as a straight line, it was created with a staircase geometry due to the gridded nature of the model.

The P-wave velocity versus depth distribution used in the modelling was generated using upscaled P-wave data from well 7121/5-1 to the E (Figs 1b, 3a). The S-wave velocity was derived by scaling the P-wave velocity from the well by 0.5, and the background density was extracted from the P-wave data using Gardner's relation (Fig. 3b, c). The displaced layer in the model was assigned a density contrast of -150 kg/m^3 relative to the background density (Figs 3f, 4a). The distribution of P- and S-wave velocities across the model are also included in Figure 3d and 3e for reference.

Forty-one sources were spaced 350 m apart and positioned at sea level (0 m depth). This geometry mimics the inline geometry of the real Snøhvit OBC survey (Fig. 1c). The sources extended to ± 7000 m horizontally across the model (Fig. 3). 1401 dual component receivers (X and Z) were placed at 300 m depth (seabed) with a 5 m spacing between ± 3500 m (Figs 3a, 4a). An isotropic pressure source with a zero-phase Tukey window wavelet consisting of a flat band between 4 and 40 Hz, and half-cosine ramps in the ranges 0-4 and 40-70 Hz was used to generate the data. Dual-component receivers were used because the analysis was only for P-S data in 2D. Free-surface-related multiples were suppressed using absorbing boundary conditions at all sides of the domain. Interbed multiples are, however, still present in the data.

During the data processing, the direct wave was muted, and the data were separated into incident angle stacks and by azimuth into E (receivers to the right of the source) and W (receivers to the left of the source) azimuths. The data in both x and z components were depth migrated using elastic reverse-time migration (Hokstad *et al.* 1998; Weibull & Arntsen 2013), with a smooth version of the velocity model from the well. The results were available in the form of PS images of the partial angle stacks for both the E and W azimuths (as in the Snøhvit data). A full incidence angle stack for the E and W azimuths (sum of all 41 sources and all incidence angles) was also generated. For an in-depth explanation of the model and data processing, as well as a complete set of individual shot-point PS images, please refer to the supplementary material.

3.2.2 Experiment 2

This experiment investigates how changes in lithology within a fault zone can colour the dominant frequencies in seismic reflections from the fault zone compared to those from the adjacent unfaulted areas (O'Doherty & Anstey 1971; Anstey & O'Doherty 2002; Weibull *et al.* 2019). It also addresses how the observed seismic frequencies of faulted reflector images may vary near to and away from the fault. As was the case for experiment 1, P-wave velocities were extracted from log data of the NO 7121/5-1 well, and S-wave velocity and density were based on the P-wave velocity as in experiment 1. (Fig. 3a-c). Also, like

experiment 1, a 300 m thick layer was vertically offset 150 m by a fault dipping 55° to the W (left of the model), and a density contrast of -150 kg/m^3 relative to the background was assigned to the displaced layer (Fig. 3f).

In this experiment, however, a 65 m thick fault zone was added using a 5 x 5 cell staircase geometry (Fig. 4b). Such a thick fault body was chosen to exaggerate how variations in the geology/elastic properties within the fault affect the seismic frequency content of the backscattered signal. It also allows us to analyse how the presence of a layered fault zone might influence the frequency content of the displaced reflectors near the fault. We used three distinct layered fault zones: a simple homogenous fault zone (Fig. 4b, top inset), and two more complex heterogeneous fault zones (Fig. 4b, middle and bottom insets). These complex zones contain 13 fault-parallel layers with different elastic properties: the first model exhibits smooth velocity transitions, while the second model has abrupt velocity transitions (Fig. 4b, middle and bottom insets).

As in experiment 1, the model contained 1401 receivers at 300 m depth (seabed) (Figs 3d-f, 4). The source-time function used in this experiment and the processing are also like experiment 1. For simplicity, the frequency content of the full stack data was analysed. Amplitude spectra were extracted from three locations for each of the models: the centre of the fault, at the intersection of the top of the horizon with the fault on the hanging wall (HW), and 800 m from the fault on the same reflector in the HW side. The S-transform of the trace was extracted from depth-to PS time converted data (Stockwell *et al.* 1996). The extraction of the trace was based on a moving and localizing Gaussian window (Stockwell *et al.* 1996). The size of this window (in time) decreases exponentially with frequency. Assuming a -40 dB cutoff, which is 1% of the peak of the window, the width of the window is ~ 0.24 s at 10 Hz, and ~ 0.08 s at 30 Hz (Eq. 1 in supplementary material). The time-frequency transformed data were then depth-converted, and the amplitude spectra were displayed for the chosen depth point in each model. For an in-depth explanation of the parameters used in this experiment please refer to the supplementary material.

The second model also has some simplifications. The modelled fault zones are thicker and simpler (layer cake) than the fault zones that can be expected in the Snøhvit field, which are likely to be thinner than 65 m and are likely to contain significant internal lateral and vertical heterogeneity (Cunningham *et al.* 2019). Despite these simplifications, the experiment can be used to examine the impact of fault zones on frequency content in and around the fault.

4. Results:

4.1 Results from the Snøhvit case study

When analysing the Snøhvit data, fault imaging is discussed with respect to discontinuity fault imaging, because there was no evidence of a seismic signal registered on the fault plane itself (Figs 1d, 5).

4.1.1 Faults and partial (incidence angle) stacks

In the Snøhvit field, the northern fault dips $\sim 54^\circ$ to the NW, and the southern fault dips $\sim 50^\circ$ to the SSW. In the reflection data, these faults are clearly visible on the crossline (N-S orientation) section (Fig. 5a). The crossline shows a discontinuity where a fault has displaced horizontal reflections, but in no partial or full stack is a fault-plane reflection observed. Tensor is the optimal attribute to image the lateral and vertical extent of the faults (Figs 5b, 6b). Both the crossline and time slice (3128 ms) from the near, mid, and far angle stacks of

the E and W datasets show high tensor values that delineate the lateral extent, width, and morphology of the faults. Imaging quality improves with increasing incidence angle stack. This is visible on the crossline section (Fig. 5b), but it is most clear on the time slice (Fig. 6b) which shows an increase in brightness, length, and width of the faults with increasing offset (this occurs regardless of azimuthal separation). Since PS reflection strength increases with increasing incidence angle (Aki & Richards, 2009), the envelope attribute exhibits an increase in magnitude and therefore amplitude with increasing incidence angle stack (Figs. 5c, 6c). The full-stack data for both the E and W datasets are most comparable to the mid-stack data but, as expected, the full stack data contain a higher signal-to-noise ratio across all the studied attributes (Figs 5, 6: Full).

4.1.2 Fault imaging versus azimuth direction

The orientations of the northern (NW dipping) and southern (SSW dipping) faults in the Snøhvit case make it possible to examine the effects of the E and W azimuthal data separation on the quality of imaging of these faults (Fig. 1c). In general, the W data exhibit longer, slightly wider, and more sharply defined tensor signals from the faults than the E data (Figs 5b and 6b). The improved imaging on the W data is much more significant for the northern fault than for the southern fault, and this is consistent across all azimuth volumes.

As tensor provides the clearest visualization of the faults, a comparison figure was made to include only partial-stack time slices of the tensor attribute (Fig. 7a-c). An AVO colour blend of the tensor attribute was also generated to understand the contribution of each partial stack (Fig. 7d). The tensor data from the W-Near compared to the E-Near reveal that the E data show slightly higher amplitude, increased sharpness, and greater lateral extent of the southern fault, compared to the W data (Fig. 7a). The northern fault is poorly imaged in near datasets, though it is slightly better resolved in the W data (Fig. 7a). In contrast, the northern fault is imaged very differently on the mid and far offset volumes, as it has higher amplitude and exhibits a longer and wider fault zone in the W data compared to the E data (Fig. 7b, c). The imaging quality also improves with increasing angle stack (Fig. 7b, c). The southern fault imaging appears to be impacted far less by azimuthal separation. It shows a slight increase in magnitude of the tensor attribute signal in the mid and far offset data from the E volume (Fig. 7b, c). However, the morphology and lateral extent of this fault is the same in both E and W datasets.

In the AVO tensor blend, faults are visualized as largely white bodies surrounded by a slight teal-blue halo, which appears to widen and extend beyond the faults' terminations (Fig. 7d). The white colour indicates that the fault is imaged by all three partial stacks in equal amounts, whereas the teal colour suggests a widening of the fault with increasing incidence angle in the mid and far data. This observation is consistent with the observations of individual stacks (Fig. 7 a-c).

4.1.3 Discontinuity imaging and seismic frequency

Frequency decomposition (FD) RGB colour blends were generated to explore the frequency content of the backscattered signal from the northern and southern faults. At the chosen 3128 ms (PS time) slice, the power spectrum (Fig. 8c, d) ranges between 3-35 Hz assuming a -20 dB cut-off. Although the power of each stack increases with incidence angle in the E and W spectra, the overall trends of all spectra are similar (Fig. 8c, d). The result of the FD are three magnitude volumes of the low, medium, and high central frequencies (8, 14 and 30 Hz). These volumes were blended into eight RGB FD colour blends, one for each of the E and W partial and full stack volumes (Fig. 8a, b).

On time slices of the FD volumes, faults appear to have significantly lower frequency content relative to the surrounding data. The faults appear as darker, almost black lineaments on each FD. Analysis of these darker bodies on several time slices reveals subtle and intermittent red-green shadows, suggesting the presence of low-medium frequency (8-14 Hz) across the entire vertical faulted interval. The adjacent areas surrounding the black fault lineaments are dominated by greenish and occasionally teal-blue haloes, which coincide with slightly higher frequency content (14-30 Hz; Fig. 8a, b). These features are observed on all the stacks regardless of azimuth or incidence angle.

In the areas away from the faults, there is a dominance of reddish (low frequency) hues with increasing incidence angle stack (Fig. 8a, b). Like the envelope attribute, the power spectra from the FD exhibit the highest amplitudes in the far-stack data (Fig. 8c, d). Also as expected, the highest frequencies (blue) are dominant in the shallowest sections of the FD volumes, and they decrease (become red) with depth (Fig. 8a, b, inlines and crosslines). The FD full-stack volumes contain the average frequency range of the near, mid, and far stacks (Fig. 8c, d).

Despite the changes in frequency being relatively unaffected by azimuth, the lateral extent of the northern fault is more clearly imaged by the W data than the E data. Conversely, the southern fault is imaged similarly in both E and W datasets and in all the partial stacks (Fig. 8). These observations suggest that the gas cloud is not affecting the azimuthal response, at least for the northern, oblique fault.

4.2 Forward seismic modelling

4.2.1 Experiment 1

The first experiment tests the effect of azimuthal separation and incidence angle on the seismic imaging of a discontinuity that offsets a layer of contrasting density (Fig. 9). The data are separated by azimuth and processed into near, mid, far, and full stacks similarly to the Snøhvit data. As result of the imaging conditions used in the experiment (supplementary material), in all stack images the top of the displaced layer is represented by a white peak at the centre surrounded by two pairs of side lobes (black-white, black-white), and it is representative of a positive PS reflection coefficient, while the base of the layer has the opposite character.

In the W data, the horizontal reflectors have a slightly brighter amplitude but also become less sharply imaged with increasing incidence angle than the E data, making it slightly more difficult to distinguish the main peak and side lobes of the horizontal reflectors (Fig. 9a-c). As there is no fault body in the model, there is no continuous reflector extending the full length of the discontinuity. However, in areas where a lateral change in density occurs (due to the fault displacement), a planar reflector is imaged.

In the E data, the brightness of the horizontal reflectors increases similarly and becomes less sharply resolved with increasing incidence angle (Fig. 9f-h). The imaging of the fault discontinuity is slightly different. In the near data (Fig. 9f), only a discontinuity is imaged, and no plane is visible, while the mid and far stacks (Fig. 9 g, h) exhibit a clear reflection from the discontinuity where brightness and reflector sharpness (i.e., a more visible main peak/trough and side lobes) increase with incidence angle.

There is almost no difference in the imaging of the horizontal reflectors between the W and E data. In contrast, the discontinuity is more clearly imaged by the W near, mid and far stacks (Fig. 9a-c in comparison to 9f-h), as demonstrated by the greater reflector strength in the W

data. In all W stacks, there is also a slight increase of amplitude at the intersections between the horizontal reflectors and the discontinuity in both the HW and footwall (FW). In the E data, these terminations are only clear in the near stack where there are no reflections from the discontinuity (Fig. 9f).

Horizon imaging is similar in the full stack data from the W and E azimuths. However, the fault discontinuity and horizons terminations at the discontinuity show some differences between the W and E full stacks (Fig. 9 d, e, i, j). As described for the partial stack data, lateral changes in density due to the presence of the discontinuity are imaged as distinct reflections. In the W data (Fig. 9 d, e), these reflections are stronger, and their character is more easily distinguished than in the E data (Fig. 9 i, j). In the W data, the horizons terminations at the discontinuity appear to be of higher amplitude than in the E data. In the W data, the discontinuity on the top of the layer is higher amplitude and more sharply defined than that on the base, while in the E data the amplitudes of the discontinuity on the top and base of the layer are comparable.

4.2.2 Experiment 2

The second experiment investigates the impact of a fault zone on the seismic frequencies observed in and surrounding the fault in three models: a simple homogenous fault, and a more complex smooth and abrupt heterogeneously layered fault (Fig. 4b, insets). The full stacked migrated images containing both E and W azimuths were converted to PS time, and they were time-frequency transformed using the S-transform (3.2.2). Amplitude spectra (Fig. 10, columns 2-4) were then analysed at the centre of the fault (red), at the HW intersection of the top of the layer with the fault (green), and ~800 m away from the fault on the same horizon in the HW (yellow) (x symbols in Fig. 10, column 1). For each one of these locations, the spectrum was extracted at a single point on the time-frequency S-transformed data (supplementary material).

In the 2D full stack for the simple-homogenous fault (Fig. 10a, column 1), the amplitude of the fault reflection changes consistently with depth between the top and base of the displaced layer, and it is controlled by the density contrast across the fault. The brightest amplitudes occur towards the top of the fault, where the layer in the FW is juxtaposed against the sequence above the layer in the HW. The lowest amplitudes occur at the middle section of the fault, where the layer is self-juxtaposed. The deepest section of the fault juxtaposes the layer in the HW against the sequence below the layer in the FW, and it is higher amplitude than the middle section of the fault, but lower amplitude than the upper section of the fault.

The reflections for the smooth and abrupt heterogeneous faults (Fig. 10 b and c, column 1, respectively) appear very similar in thickness, length, and strength, and they are more controlled by the internal structure of the fault. As expected, the abrupt model has more clearly imaged the fault internal geometry, since this model has more contrast in the elastic properties of the fault.

The extracted spectra from within the fault (Fig. 10, red x and column 2) show an increase in dominant frequency with increasing fault complexity. The amplitude spectrum for the homogeneous fault zone shows a peak in the low frequency signal (5-15 Hz, 0.2-0.4 magnitude) and a decrease towards medium-high frequencies (15-70 Hz, 0-0.2 magnitude; Fig. 10a, column 2). The power spectrum of the heterogeneous smooth fault zone has a peak of medium frequency content (~23 Hz, decreasing towards 70 Hz) and relatively little low frequency content (Fig. 10b, column 2). Finally, the power spectrum for the heterogeneous

abrupt fault zone has a peak at higher frequency (30 Hz, decreasing towards 70 Hz) and little low frequency content (4-20 Hz, Fig. 10c, column 2).

The spectra of the top of the layer immediately adjacent to the fault in the HW (Fig. 10, green x and column 3) exhibit higher frequencies than those observed away from the fault (Fig. 10, yellow x and column 4), and the dominant frequency increases with increasing fault complexity. In the homogeneous fault (Fig. 10a, columns 3 and 4), a peak of low frequency followed by a plateau of medium-high frequencies (10 and 25-50 Hz respectively) occur at the HW cutoff, while away from the fault, the reflector exhibits relatively consistent contributions from all frequencies. The heterogeneous smooth and complex abrupt cases show more significant differences with a higher abundance of medium (~15-25 Hz) and high (~30-50) frequencies at the HW cutoff (Fig. 10b and c, column 3), compared to the spectra away from the fault (Fig. 10b and c, column 4). The spectra extracted far from the fault in the HW are similar for the three models and are unaffected by fault complexity (Fig. 10a-c, column 4). These results suggest a linkage between the reflector frequencies adjacent to the fault and the internal morphology of the fault zone, which will be discussed further in section 5.4.

Since the model lacks realistic elastic properties for the fault and layer boundaries, we cannot compare the modelling results directly with the Snøhvit data. Despite this, it is interesting that higher frequencies are consistently seen in data close to the fault relative to away from it, indicating that the presence of a layered fault zone affects the frequency content of horizons close to the fault, and that increasing fault complexity results in an increase in reflection strength throughout most of the spectrum.

5. Discussion:

5.1 The imaging of faults in the Snøhvit data

The modelling experiments (Fig. 9) demonstrate that the Snøhvit data should have had adequate illumination to image the faults as reflections. However, the analysis of the PS data (Fig. 5a) showed no evidence of fault-plane imaging as a distinct reflection. Faults in the dataset are imaged as horizon discontinuities only. There are several possible explanations for this.

The first possible reason is the survey geometry. If the incidence angles are collected in a narrow range and/or the survey is not large enough, it is possible that waves reflecting off the fault would not be returned to receivers. This effect is evident in the E-Near modelled data where some individual shot points capture fault discontinuity imaging but no reflections (Fig. 9f). Despite the large inline offset of the Snøhvit survey, and the wide range of incidence angles (0-65°), the crossline offsets are quite limited (typically in the range between 600-1175 m). The limited crossline aperture of the survey geometry could thus have played a role in the lack of fault reflection imaging in the Snøhvit data, especially where faults are oblique to the inline direction.

The next possible explanation for the lack of fault reflections involves the processing workflow applied to the Snøhvit data. Injudicious parameterization and application of data processing modules can sometimes discriminate against weak signals, and dipping events are no exception to that. In the workflow of Table 1, it is possible that the Radon demultiple stages (steps 18 and 28) removed the reflections from the dipping fault planes (e.g. Yilmaz 2001). However, since processors seek to retain dipping events, such as diffractions, for optimal migration, this explanation seems unlikely.

Another reason that might have caused the lack of fault reflections is the geology itself. In the forward models, the only way to avoid imaging the fault was by applying a smooth elastic properties transition across this boundary. It is possible that the studied faults have smooth elastic property transitions which reduce their reflection strength. However, the size and variations in lithology across the Snøhvit faults (Cunningham *et al.* 2019) make this very unlikely. Unfortunately, without wellbores transecting the fault zones, it is impossible to conclude on the reason for the missing fault reflections. The remainder of the discussion will focus on the imaging of the faults as discontinuities.

5.2 Incidence angles

In the Snøhvit data, imaging of the northern fault improves with increasing incidence angle in both the E and W azimuths (Fig. 7), whereas it is relatively unchanged with respect to fault length and morphology for the southern fault. The discontinuity appeared to widen and lengthen with increasing incidence angle as depicted in the AVO colour blend of tensor by a teal halo (Fig. 7d). With an increase in incidence angle, the PS data exhibits a systematic increase in the strength and a decrease in frequency of reflections across the study area (Figs. 5c, 6c, envelope attribute and Fig. 8). The increase in PS reflection amplitude with incidence angle is both well understood and to be expected, going as sine of the incidence angle at small angles (Aki & Richards, 2009). The decrease in dominant frequency with increase in incidence angle can be explained by a combination of higher intrinsic attenuation due to the larger propagation distances, and migration stretch associated with steeper travel-time curves at wider angles.

The amplitudes of the top and base layer-boundaries in experiment 1 increased with increasing incidence angle but also appear to be less sharply resolved. No fault zones were included in this model, and the discontinuity created lateral changes in the elastic properties which were imaged as reflections. There were no observed systematic changes which could be linked to increasing incidence angle for the discontinuity plane. To better illustrate the discontinuity plane imaging, the envelope of the lateral gradient was computed on the modelled partial and full stack data (Fig. 11). This measurement shows a strengthening of the lateral gradient envelope from the discontinuity plane with increasing incidence angle for the E data, and a decrease with increasing incidence angle for the W data (Fig. 11).

Experiment 1 provides an explanation for the changes in amplitude and imaging quality with increasing incidence angle. The envelope attribute in the case study (Fig. 5c, 6c) confirms that PS reflection strength increases with increasing incidence angle across the entire study area. It is proposed that this change in reflector strength is responsible for the improved imaging of the faults with increasing angle stack, which was observed in the tensor attribute for the Snøhvit data.

5.3 Azimuthal Separation

The Snøhvit data exhibit a clear linkage between the orientation of the narrow-swath seabed survey (E-W), the orientation of the faults, and the resulting discontinuity imaging (Fig. 7). The northern fault is oriented oblique to the seismic acquisition direction and is more clearly imaged in the W data than in the E data. The southern fault is oriented approximately parallel to the survey, and it shows very little difference between the E and W azimuths.

Experiment 1 demonstrates that the W azimuth data were generally better at imaging the W dipping fault than the E data (Fig. 9). Despite the absence of a distinct fault zone in this experiment, the fault was imaged due to contrasts in elastic properties across the fault. In

addition, the quality of the discontinuity plane imaging appears to be linked to the increase in amplitude where the reflector terminates at the fault. A ray-tracing study was conducted on the model to understand the contribution of seismic signal coming from a single point on the upper fault plane, and to see how that single point is illuminated by individual shot points (Fig. 12). The point is treated as a reflecting point under Snell's law, and the rays are limited to a maximum incidence angle (θ , with respect to the horizontal) of 65° (the maximum θ in the Snøhvit data) and the lateral extent of the receivers at the seafloor (more details about the ray tracing methodology are given in the supplementary material). By counting the azimuthally separated ray paths in the ray-tracing diagram, the W azimuth has far more single shots returning signal to the receivers than the E azimuth (Fig. 12a).

Raytracing was used to extract shot-point position and incidence angle with respect to the normal to the fault plane (θ_f) vs. the reflection coefficient (R_{ps}), which was estimated from the amplitude of the ray-traced data using the Zoepritz equation (Fig. 12b, c). In the W data, a reflection was returned from shot points ranging between -300 and -2050 m for the single point on the fault plane, while the E data cover only shot points between -2050 to -2600 m (Fig 12b). This is the result of the survey geometry, and the fact that the source lines are twice as long (14 km) than the receiver lines (7 km, Fig. 3d). In θ_f versus reflection coefficient, the W data was able to return a reflection for θ_f of $-45-0^\circ$, while the E data were only imaged in the nearest θ_f , $0-10^\circ$ (Fig. 12c). Thus, the rays are clearly dominated by W azimuth reflections. Although this analysis is just for a single point, it confirms the impact of seismic survey orientation relative to the structures and azimuthally separating data on the imaging of faults.

The discontinuity also impacts the imaging of reflector terminations in the model and like the Snøhvit data, the effects are more obvious in the W data. Experiment 1 showed little difference in the imaging of the top and base layer boundaries, while the terminations of these reflections with the discontinuity strengthen and even change orientation slightly from horizontal. The signal of these terminations appeared strongest when the seismic imaging of the fault was strongest in the W data (Fig. 9a). Similarly, the E-near data shows no image of a fault plane, and no change in amplitude where the discontinuity intersects the horizons (Fig. 9f). When a seismic wave (P or S) reflects off a structural edge such as a fault, both specular and diffracted waves are generated (i.e. Landa & Keymar 1998). Specular waves are conventionally used to image and interpret structural or stratigraphic features. However as discussed before, no evidence of fault plane reflections (specular waves) is seen in the Snøhvit data. Difractions, a common aspect of fault imaging, are scattered from a single point or edge when a seismic wave interacts with a discontinuity (Landa & Keymar 1998; Taner *et al.* 2006; Landa 2012; Fomel *et al.* 2018). The increase in amplitude and slight signal variation at the reflector cutoff is interpreted to be a consequence of the interplay between diffractions from the fault and the reflection of the horizontal surface (see videos in supplementary material). Experiment 1 shows that there is an interplay between the fault orientation, the survey orientation, and the interaction of seismic waves (and therefore the generation of diffractions) which may cause changes to the imaging of faults with azimuth. It is not possible to comment on the impact of swath narrowness in the Snøhvit case study since we have only used 2D modelling.

Complex fault zones are likely to be present in the Snøhvit field and waves scattered by them are expected to superpose reflections from adjacent horizons. In the Snøhvit data, the northern fault is oblique to the survey and, compared to the southern fault, it is expected that the HW side of this fault is better illuminated. The more P-waves that interact with the HW, the more specular P- / S- waves and diffractions reflect and scatter off the fault. If these

diffractions subtly modify/increase the amplitude and possibly alter the boundary reflections adjacent to the fault, the tensor (and other discontinuity-enhancing attributes) signal will change. This subtle difference in the lateral contrast of the signal created by diffractions could be responsible for the differences in tensor attribute that are seen in the Snøhvit data, where the imaging afforded by discontinuities in the W data is clearly stronger than that from the E data. In the E data, we see less of this phenomenon since more of the specular and diffracted energy is lost due to the placement of the source and receivers relative to the fault. For the E data, the fault signal occurs where the seismic wave reflects off the FW side of the fault, but in this case the reflected signal does not return to the receivers since they are in the opposite direction. This subtle difference in the lateral contrast of the signal created by diffractions can also explain why the southern (survey parallel) fault is almost identical in the E and W datasets.

5.4 The frequency content of faults in seismic

Frequency decompositions in the Snøhvit data show the faults as black lineaments with a lower frequency content than the adjacent areas. Within these dark lineaments, there were subtle shadows of low-medium frequency (8-12 Hz) content in all partial and azimuthally separated datasets (Fig. 8). Haloes of high frequency (14-30 Hz) were observed in the areas next to the faults, which correlate with the termination of the discontinuity (fault zone) with the imaged horizons. Farther away from the faults, in areas that appear undisturbed by faulting, the frequency is low (< 8 Hz), and the proportion of low frequencies increases with increasing incidence angle stack (Fig. 8). Seismic waves decrease in frequency content with increasing depth, so for the interval being investigated in the frequency decompositions (3128 ms, PS time), the abundance of low-frequency data away from the faults is expected (Stewart & Lawton 1996).

Experiment 2 tests these observations by comparing a simple homogenous and two heterogeneous layered faults with smooth and abrupt velocity variations (Figs 10 and 4b). Three frequency extractions were taken from each of the seismic sections: one in the fault zone, one in the HW termination of the fault with the top of the layer, and one in the same boundary ~800 m away from the fault on the HW side (Fig. 10). In the fault zone, the frequency increased with fault zone complexity suggesting a linkage between the geological complexity of the fault zone and the dominant frequency value (Fig. 10, red x). At the termination of the fault zone with the top of the layer an increase in frequency with fault complexity was also observed (Fig. 10, green x). 800 m away from the fault in the HW, there was no observed change in frequency with fault complexity (Fig. 10, yellow x). Though there is a chance for spectral leakage in this experiment, the window size at the dominant frequencies close to the fault in the complex fault zone models (20 to 50 Hz; Fig. 10 b, c, third column) is rather small (0.12 to 0.05 s; Eq. 1 in supplementary material). Therefore, we consider the possibility of spectral leakage at the points within or close to the fault (red and green points in Fig. 10) to be insignificant, particularly for the case of a complex fault zone.

In the Snøhvit data, the observed frequencies from within the fault zone are less obvious than in experiment 2 since faults and boundaries in these models are largely exaggerated. We did observe slightly higher frequencies in the areas adjacent to the faults (fault zones) relative to the unfaulted areas in the Snøhvit data, but this relationship is not as obvious as in the models. From the observations in the Snøhvit data and experiment 2, we conclude that fault zones and the dominant frequencies attained in their imaging can influence the frequency content of adjacent seismic reflectors.

The reasons for the relative increase in high frequency content in areas affected by the faults (fault zones) are not fully understood, although some hypotheses are presented here. Fault zones are complex, heterogeneous rock bodies that have undergone large strain which can affect the mechanical and elastic properties of the fault rock. The observed increasing shift in dominant frequency in and around the faults is interpreted to be related to abrupt variations in elastic properties within the fault zone, which could be due to lithological variation. Smooth lithological changes result in lower dominant frequencies than abrupt changes (Fig. 10). The seismic response of a subsurface model is approximately obtained by a convolutional process where the source wavelet is filtered by the impulse response of the model. It is possible for a periodically layered subsurface structure to colour the spectrum of an incident pulse so that it behaves as a bandpass filter. This work suggests that low frequency scattered signals can be obtained from a homogeneous fault zone (Fig. 10a), while scattered high frequencies can be obtained using fault zone models with more abrupt changes in elastic properties (Fig. 10b, c). These findings are consistent with the findings of Iacopini *et al.* (2012) and well-known theories (Aki, 1982) in signal processing/filtering.

Seismic frequencies from imaged faults can have a great effect on the imaging of horizontal reflector terminations at the fault. This is observed in both the Snøhvit data and the modelled data as high-frequency haloes and spectral extractions, respectively. O'Doherty & Anstey (1971) supported the concept that lithological changes and layering can colour spectral amplitudes from thin beds which are tuned at specific frequencies (Widess 1973; Partyka *et al.* 1999). Our study opted to test further the impact of layering on the frequencies observed in and near faults. Higher frequencies were observed in areas next to the faults in the Snøhvit case study (Fig. 8) and in the two complex fault experiments (Fig. 10b, c). Although it is much more difficult to verify on real seismic data, it is likely that both tuning thickness and changes in mechanical properties played a role in colouring higher frequencies around the studied faults (Weibull *et al.* 2019). Alaei & Torabi (2017) used frequency decompositions to generate a high-frequency magnitude volume from seismic which was used as the most successful parameter in the imaging of faults. Their findings support the observations from the Snøhvit data, where the areas adjacent to the faults (fault zones) are more clearly imaged on higher frequency data and exhibit higher frequency than the unfaulted areas. It is possible that more detailed seismic modelling could improve our understanding of these frequency anomalies, although given the limited resolution of seismic data and the lack of information (well data) about fault zone properties, it may be challenging to reach a firm explanation for these observations.

6. Conclusions and Implications

This paper examines the effects of azimuthal separation and incidence angle on fault imaging. It also investigates the effect of frequency on fault imaging. PS data from the Snøhvit field were used as they are much less affected by the presence of shallow gas in the overburden when compared to the PP data. Both the case study and modelling showed that fault imaging quality (brightness, length, and width) varies systematically with azimuth. In general, the two studied faults were imaged more clearly in the W azimuth data than they were in the E data, especially the northern fault, which is oblique to the survey orientation. Azimuthal separation is shown to be a valuable method to study faults that are oriented oblique to orthogonal to the survey orientation, especially when the survey is narrow swath as in Snøhvit. When faults are parallel to the acquisition direction, such as the southern fault in our case study, there are few differences between the data collected from two diametrically opposed azimuths.

The Snøhvit data showed improved imaging of fault discontinuities with increasing incidence angle stacks (Fig. 7). With increasing incidence angle, the observed increase in reflector strength is most likely responsible for the improvements to fault imaging, as seen in the tensor attribute with incidence angle. The same conclusion is apparent in the results of modelled data (Fig. 9).

Finally, a study on frequency showed fault images in the Snøhvit field to be dominated by low-medium frequency shadows, with haloes of medium-high frequencies surrounding the fault lineaments (Fig. 8). The modelled seismic data confirm that complex fault morphologies resulted in higher frequencies in the fault-zone image than their less complex counterparts (Fig. 10). This relative increase in dominant frequency may be attributed to tuning effects in the heterogeneous fault zones. The tuning effects vary according to the smoothness of the transition in the acoustic properties (due to variations in, for example, lithology). The modelled data also showed that regardless of fault complexity, the spectra estimated from imaged reflectors near a fault are also coloured by the spectral content of the fault image.

Several recommendations are made based on the results of this study that can be applied to processing and interpretation workflows.

Processing: azimuthal separation has great potential to be applied to fault characterization and structural analysis. If a narrow-swath survey is approximately perpendicular to the fault trend, it is highly advantageous to separate the diametrically opposed azimuths along the survey, especially in developing the migration velocity model. Azimuthally separated data reveal contrasts in the resulting fault imaging (fault length, morphology), and it can highlight the effects of specular versus diffracted wave imaging. Routine generation of incidence-angle stacks is also critical in areas where detailed fault interpretation is necessary, as seen in the overall increase in fault image quality with increasing incidence angle in the Snøhvit case study.

Interpretation: an understanding of the survey design is critical when interpreting faults in OBS seismic data. Interpretation on azimuthally separated volumes and incidence-angle cubes results in improved understanding of faults in the subsurface, compared to interpretation on only a full stack, full-azimuth seismic volume.

These results contribute to the understanding of how faults are imaged, and how survey geometry, processing techniques and frequency can influence fault imaging in PS data. This work may also improve the quality and accuracy of fault interpretation in OBS data. Since OBS surveys are becoming more frequently used in both exploration and production (e.g. Claire, Ekofisk, Grane, Gullfaks, Johan Sverdrup, Oseberg and Valhall Fields; Barkved *et al.* 2005; Haugvaldstad *et al.* 2011; Bertrand *et al.* 2014; Eriksrud 2014; Eriksen 2018), it is vital that geoscientists understand how PP and PS data are acquired and processed, and how seismic waves might interact with structures to extract the greatest amount of information from the subsurface.

Acknowledgements

The authors would like to thank the Norwegian Ministry of Education and Research for funding this research. Thanks to Equinor ASA and their partners in the Snøhvit field, Petoro AS, Total E&P Norge AS, Neptune Energy AS, and Wintershall Dea AS for providing the seismic data used in this study. We would also like to thank Geoteric for providing us with the licenses for their softwares (2018) and their support. A special thanks to Jim Brown, Gard Ole Wærum, Henrietta Sørensen, Bård Osdal and Richard Callow for their scientific

contributions to this paper. Careful review by the co-editor and an anonymous reviewer greatly improved the manuscript.

References

- Aki, K. 1982. Scattering and attenuation. *Bull. Seis. Soc. Am.*, **72**, S319-S330, <https://doi.org/10.1785/BSSA07206B0319>.
- Aki, K. & Richards, P.G. 2009. Quantitative Seismology, second edition. University Science Books, 700 p.
- Alaei, B. & Torabi, A. 2017. Seismic imaging of fault damaged zone and its scaling relation with displacement. *Interpretation*, **5**, <https://doi.org/10.1190/int-2016-0230.1>.
- Anstey, N.A. & O'Doherty, R.F. 2002. Cycles, layers, and reflections: Part 1. *Leading Edge*, **21**, 44–51, <https://doi.org/10.1190/1.1445847>.
- Bakker, P. 2002. *Image Structure Analysis for Seismic Interpretation*. Technische Universiteit Delft.
- Barkved, O.I., Buer, K., Kristiansen, T.G., Kjelstadli, R.M. & Kommedal, J.H. 2005. Permanent seismic monitoring of the Valhall field, Norway. *2005 International Petroleum Technology Conference Proceedings*, 1523–1527.
- Barr, F.J. 1997. Dual-sensor OBC technology. *The Leading Edge*, **16**, 45–52, <https://doi.org/https://doi.org/10.1190/1.1437427>.
- Bertrand, A., Folstad, P.G., et al. 2014. Ekofisk life-of-field seismic: Operations and 4D processing. *The Leading Edge*, **33**, 142–148.
- Botter, C., Cardozo, N., Hardy, S., Lecomte, I. & Escalona, A. 2014. From mechanical modeling to seismic imaging of faults: A synthetic workflow to study the impact of faults on seismic. *Marine and Petroleum Geology*, **57**, 187–207, <https://doi.org/10.1016/j.marpetgeo.2014.05.013>.
- Botter, C., Cardozo, N., Hardy, S., Lecomte, I., Paton, G. & Escalona, A. 2016. Seismic characterisation of fault damage in 3D using mechanical and seismic modelling. *Marine and Petroleum Geology*, **77**, 973–990, <https://doi.org/10.1016/j.marpetgeo.2016.08.002>.
- Botter, C., Cardozo, N., Qu, D., Tveranger, J. & Kolyukhin, D. 2017a. Seismic characterization of fault facies models. *Interpretation*, **5**, 1–18.
- Botter, C., Cardozo, N., Lecomte, I., Rotevatn, A. & Paton, G. 2017b. The impact of faults and fluid flow on seismic images of a relay ramp over production time. *Petroleum Geoscience*, **23**, 17–28.
- Chopra, S. & Marfurt, K.J. 2007. Seismic Attributes for Prospect Identification and Reservoir Characterization. Society of Exploration Geophysicists, Geophysical Developments No. 11, Tulsa.
- Cunningham, J., Cardozo, N., Townsend, C., Iacopini, D. & Wærum, G.O. 2019. Fault deformation, seismic amplitude and unsupervised fault facies analysis: Snøhvit Field, Barents Sea. *Journal of Structural Geology*, **118**, 165–180, <https://doi.org/10.1016/j.jsg.2018.10.010>.

- Dawers, N.H. & Underhill, J.R. 2000. The role of fault interaction and linkage in controlling synrift stratigraphic sequences: Late Jurassic, Statfjord East area, northern North Sea. *AAPG Bulletin*, **84**, 45–64.
- Elliott, G.M., Wilson, P., Jackson, C.A.L., Gawthorpe, R.L., Michelsen, L. & Sharp, I.R. 2012. The linkage between fault throw and footwall scarp erosion patterns: An example from the Bremstein Fault Complex, offshore Mid-Norway. *Basin Research*, **24**, 180–197.
- Ensley, R.A. 1984. Comparison of P- and S-wave seismic data - A new method for detecting gas reservoirs. *Geophysics*, **49**, 1420–1431, <https://doi.org/10.1190/1.1441771>.
- Eriksen, E. 2018. Contract for improved recovery on Johan Sverdrup. *Equinor ASA Website*<https://www.equinor.com/en/news/17jan2018-johan-sverdrup.html>.
- Eriksrud, M. 2014. Seabed permanent reservoir monitoring (PRM) - A valid 4D seismic technology for fields in the North Sea. *First Break*, **32**, 67–73.
- Farfour, M. & Yoon, W.J. 2016. A review on multicomponent seismology: A potential seismic application for reservoir characterization. *Journal of Advanced Research*, **7**, 515–524, <https://doi.org/10.1016/j.jare.2015.11.004>.
- Fomel, S., Landa, E. & Turhan Taner, M. 2018. Post-stack velocity analysis by separation and imaging of seismic diffractions. *Society of Exploration Geophysicists - SEG International Exposition and 76th Annual Meeting 2006, SEG 2006*, 2559–2563.
- Garotta, R. & Granger, P.Y. 1988. Acquisition and processing of 3C × 3- D data using converted waves. In: *SEG Technical Program Expanded Abstracts*. 995–997, <https://doi.org/10.1190/1.1892469>.
- Gomez, L. 2015. AVO Screening (Part 2): AVO colour blends. *Geoteric Blog*. <https://blog.geoteric.com/technical/part2-avo-screening>
- Granli, J.R., Arntsen, B., Sollid, A. & Hilde, E. 1999. Imaging through gas-filled sediments using marine shear-wave data. *Geophysics*, **64**, 668–677, <https://doi.org/10.1190/1.1444576>.
- Gray, D. 2008. Fracture detection using 3D seismic azimuthal AVO. *CSEG Recorder* **33**(3), 40–49.
- Han, C. 2017. Frequency Decomposition Part 2- Constant Q. *Geoteric Blog*<https://blog.geoteric.com/frequency-decomposition-part-2-constant-q>.
- Haugvaldstad, H.H., Lyngnes, B., Smith, P. & Thompson, A. 2011. Ekofisk time-lapse seismic- a continuous process of improvement. *First Break*, **29**, 113–120.
- Hokstad, K., Mittet, R. & Landrø, M. 1998. Elastic reverse time migration of marine walkaway vertical seismic profiling data. *Geophysics*, **63**, 1685–1695, <https://doi.org/10.1190/1.1444464>.
- Iacopini, D. & Butler, R.W.H. 2011. Imaging deformation in submarine thrust belts using seismic attributes. *Earth and Planetary Science Letters*, **302**, 414–422, <https://doi.org/10.1016/j.epsl.2010.12.041>.

- Iacopini, D., Butler, R.W.H. & Purves, S. 2012. Seismic imaging of thrust faults and structural damage: A visualization workflow for deepwater thrust belts. *First Break*, **30**, 77–84, <https://doi.org/0.3997/1365-2397.30.5.58681>.
- Iacopini, D., Butler, R., Purves, S., McArdle, N. & De Freslon, N. 2016. Exploring the seismic expression of fault zones in 3D seismic volumes. *Journal of Structural Geology*, **89**, 54–73.
- Jenner, E. 2002. Azimuthal AVO: Methodology and data examples. *The Leading Edge*, **21**, 782–786, <https://doi.org/10.1190/1.1503184>.
- Jilinski, P. & Wooltorton, T. 2016. Comparison of spectral enhancement techniques and application to improved well-to-seismic ties. In: *GeoConvention 2016*. Calgary, Canada, 1–4.
- Landa, E. 2012. Seismic diffraction: where's the value? *SEG Technical Program Expanded Abstracts*, 1–4. <https://doi.org/10.1190/segam2012-1602.1>
- Landa, E. & Keymar, S. 1998. Seismic monitoring of diffraction images for detection of local heterogeneities. *Geophysics*, **63**, 1093–1100.
- Landrø, M. & Amundsen, L. 2010. Marine Seismic Sources Part 1. *GEOExPro* 7, 32-37.
- Landrø, M. & Amundsen, L. 2018. *Introduction to Exploration Geophysics and Recent Advances*, 1st ed. Whaley, J. (ed.). Bivrost.
- Linjordet, A. & Olsen, R.G. 1992. The Jurassic Snøhvit gas field, Hammerfest basin, offshore northern Norway. In: *Giant Oil and Gas Fields of the Decade 1978-1988*. American Association of Petroleum Geologists, 349–370.
- Long, J.J. & Imber, J. 2012. Strain compatibility and fault linkage in relay zones on normal faults. *Journal of Sedimentary Petrology*, **36**, 16–26, <https://doi.org/10.1016/j.jsg.2011.12.013>.
- Mohammedyasin, S.M., Lippard, S.J., Omosanya, K.O., Johansen, S.E. & Harishidayat, D. 2016. Deep-seated faults and hydrocarbon leakage in the Snøhvit Gas Field, Hammerfest Basin, Southwestern Barents Sea. *Marine and Petroleum Geology*, **77**, 160–178, <https://doi.org/10.1016/j.marpetgeo.2016.06.011>.
- O'Doherty, R.F. & Anstey, N.A. 1971. Reflections on Amplitudes. *Geophysical Prospecting*, **19**, 430–458.
- Osagiede, E.E., Duffy, O.B., Jackson, C.A.L. & Wrona, T. 2014. Quantifying the growth history of seismically imaged normal faults. *Journal of Structural Geology*, **66**, 382–399, <https://doi.org/10.1016/j.jsg.2014.05.021>.
- Ostanin, I., Anka, Z., di Primio, R. & Bernal, A. 2012. Identification of a large Upper Cretaceous polygonal fault network in the Hammerfest basin: Implications on the reactivation of regional faulting and gas leakage dynamics, SW Barents Sea. *Marine Geology*, **332–334**, 109–125, <https://doi.org/http://dx.doi.org/10.1016/j.marpetgeo.2012.03.005>.
- Partyka, G., Gridley, J. & Lopez, J. 1999. Interpretational applications of spectral decomposition in reservoir characterization. *The Leading Edge*, **18**, 353–360,

<https://doi.org/10.1190/1.1438295>.

Perez, G. & Marfurt, K.J. 2007. New azimuthal binning for improved delineation of faults and fractures. *Geophysics*, **73**, S7-S15, <https://doi.org/10.1190/1.2813136>.

Stewart, R.R. & Lawton, D.C. 1996. *P-S Seismic Exploration : A Mid-Term Overview*. CREWES research report 8, 1-34.

Stewart, R.R., Gaiser, J.E., Brown, R.J. & Lawton, D.C. 2002. Tutorial Converted-wave seismic exploration : Methods. *Geophysics*, **67**, 1348–1363, <https://doi.org/10.1190/1.1512781>.

Stewart, R.R., Gaiser, J.E., Brown, R.J. & Lawton, D.C. 2003. Tutorial Converted-wave seismic exploration : Applications. *Geophysics*, **68**, 40–57, <https://doi.org/10.1190/1.1512781>.

Stockwell, R.G., Mansinha, L. & Lowe, R.P. 1996. Localization of the Complex Spectrum: The S-Transform. *IEEE Transactions on Signal Processing*, **44**, 998–1001, <https://doi.org/10.1109/78.492555>.

Taner, M.T., Fomel, S. & Landa, E. 2006. Separation and imaging of seismic diffractions using plane- wave decomposition. Society of Exploration Geophysicists Technical Program Expanded Abstracts 2401–2405, <https://doi.org/10.1190/1.2370017>.

Torabi, A., Alaei, B. & Kolyukhin, D. 2017. Analysis of fault scaling relations using fault seismic attributes. *Geophysical Prospecting*, **65**, 581–595, <https://doi.org/10.1111/1365-2478.12440>.

Tvedt, A.B.M., Rotevatn, A., Jackson, C.A.L., Fossen, H. & Gawthorpe, R.L. 2013. Growth of normal faults in multilayer sequences: A 3D seismic case study from the Egersund Basin, Norwegian North Sea. *Journal of Structural Geology*, **55**, 1–20, <https://doi.org/10.1016/j.jsg.2013.08.002>.

Virieux, J. 1986. P-SV wave propagation in heterogeneous media. *Geophysics*, **51**, 889–901, <https://doi.org/10.1190/1.1442147>.

Weibull, W.W. & Arntsen, B. 2013. Automatic migration velocity analysis using reverse-time migration. *Geophysics*, **55**, 1070–1088.

Weibull, W.W., Ahmad, S.S., Brown, R.J., Rosland, B. & Nazi, H. 2019. A comparison of the effects of layering and attenuation on the seismic response of gas reservoirs. *81st EAGE Conference and Exhibition, London, Extended Abstract Tu_R02_14*, <https://doi.org/0.3997/2214-4609.201900805>.

Widess, M.B. 1973. How thin is a thin bed? *Geophysics*, **38**, 1176–1180.

Xu, X. & Tsvankin, I. 2007. A case study of azimuthal AVO analysis with anisotropic spreading correction. *The Leading Edge*, **26**, 1552–1561, <https://doi.org/10.1190/1.2821942>.

Yilmaz, O. 2001. *Seismic Data Analysis: Processing, Inversion, and Interpretation of Seismic Data*, 2nd ed. Tulsa, OK, United States of America, Society of Exploration Geophysicists.

Figure Captions

Figure 1: (a) The Hammerfest Basin and its bounding areas. The area in b is marked by a black box. Modified from NPD Fact maps. (b) Hammerfest basin (blue background) and Lower-Middle Jurassic gas fields (red). The orange square is the study area at the western margin of the Snøhvit field. The orange dashed line is the crossline pictured in (c). Map modified from Linjordet & Olsen (1992) and Ostanin *et al.* (2012). (c) The survey setup. The longer red lines represent the shooting lines, and the purple lines housed in green boundaries are the ocean bottom cables and swaths respectively. (d) Crossline from the E full stack data volume with marker horizon placement for reference. (e) Generalized lithostratigraphic column of the Barents Sea with same marker horizon references as seen in (d). Modified from Ostanin *et al.* (2012). The northern (light blue) and southern (green) faults are overlaid for reference in b, c and d.

Figure 2: A pure P-wave reflection compared with the reflection of a converted PS-wave. Notice the difference between the mid-point (MP) of the pure P-wave, and the conversion point (CP) of the converted-wave. The incidence angle i of the P-wave and the reflection angle j of the S-wave also differ. Modified from Stewart *et al.* (2002).

Figure 3: P-wave velocity (a) S-wave velocity (b) and density curves extracted from well 7121/5-1 and the respective V_p (d), V_s (e) and density (f) models.

Figure 4: Geological models for the synthetic seismic experiments. (a) Experiment 1 tests the effects of source location relative to the fault and azimuthal separation. This model shows a discontinuity that resembles a fault, but the fault body is not modelled. (b) Experiment 2 tests the seismic frequency contained in a simple, homogeneous fault (top inset) and two more complex heterogeneous faults (middle and bottom insets). The fault zone is 65 m wide and exhibits a multi-layer morphology in the two heterogeneous fault zones. Graphs of the velocity transitions across the fault zones are also included.

Figure 5: Partial (near, mid, far) and full stacks of the W and E (a) reflection data, (b) tensor and (c) envelope attributes displayed on a crossline through the centre of the study area (Fig. 1c).

Figure 6: Partial (near, mid, far) and full stacks of the W and E (a) reflection data, (b) tensor and (c) envelope attributes displayed on time slice 3128 ms (PS time). This slice is approximately at the middle of the main faulted interval (Fig. 1d).

Figure 7: Comparison of time slices of the W (left) and E (right) tensor attribute for the (a) near, (b) mid, and (c) far offsets and an RGB AVO colour blend (d) of the near (Red), mid (Green) and far (Blue) tensor attributes. These are all displayed on a time slice at 3128 ms (PS time).

Figure 8: Frequency decomposition of the E (a) and W (b) data for the near (column 1), mid (column 2), far (column 3) and full stacks (column 4). Power spectra of the E (c) and W (d) near (blue line), mid (green), far (red) and full (black) 3128 ms time slices. The frequency decompositions were generated using central frequency magnitude volumes of 8, 14 and 30 Hz (c, d; grey dashed lines). The frequency data are displayed in PS time on an inline, crossline and time slice (3128 ms).

Figure 9: Synthetic seismic experiment 1. The models are separated into W/E azimuth (left/right columns) and incidence angle stacks: near (a/f), mid (b/g), far (c/g), full (d/i), and full

with layer boundaries overlaid (**e/j**). The figures focus on the fault area indicated by the black rectangle on the geological model.

Figure 10: Synthetic seismic experiment 2. A simple (homogeneous) and two more complex (heterogeneous) fault zone models (Fig. 4b) were used to generate three different full stack/azimuth seismic volumes and frequency extractions. The resulting full stack/azimuth seismic and amplitude spectra for the simple (**a**), the heterogeneous-smooth (**b**) and heterogeneous-abrupt fault models (**c**). The locations where the amplitude spectra were extracted are marked with a green, red and yellow x. These extraction points refer to the middle of the fault zone (red), the HW cutoff of the reflector (green), and the unfaulted reflector in the HW (yellow).

Figure 11: Envelope of the lateral gradient attribute of experiment 1. The attributes are separated into W/E azimuth (left/right column) and by incidence angle stacks: near (**a/f**), mid (**b/g**), far (**c/h**), full (**d/i**), and full with layer boundaries overlaid (**e/j**). The data are also separated into W (**left column**) and E (**right column**) azimuths. The figures focus on the fault area indicated by the black rectangle on the geological model.

Figure 12: Ray tracing study: (**a**) ray tracing of a single point on the upper boundary of the discontinuity plane, the rays are coloured by azimuth. (**b**) Shot point vs. PS reflection coefficient and (**c**) incidence angle (θ_f) vs. PS reflection coefficient. Notice that θ_f is measured with respect to the normal to the fault. Negative θ_f refers to west data where the rays hit the fault east of the normal and reflect west of the normal, and vice versa.

Table 1: The processing workflow for the Snøhvit data as provided from Equinor and their partners in the Snøhvit field.

ACCEPTED MANUSCRIPT

Figure 1

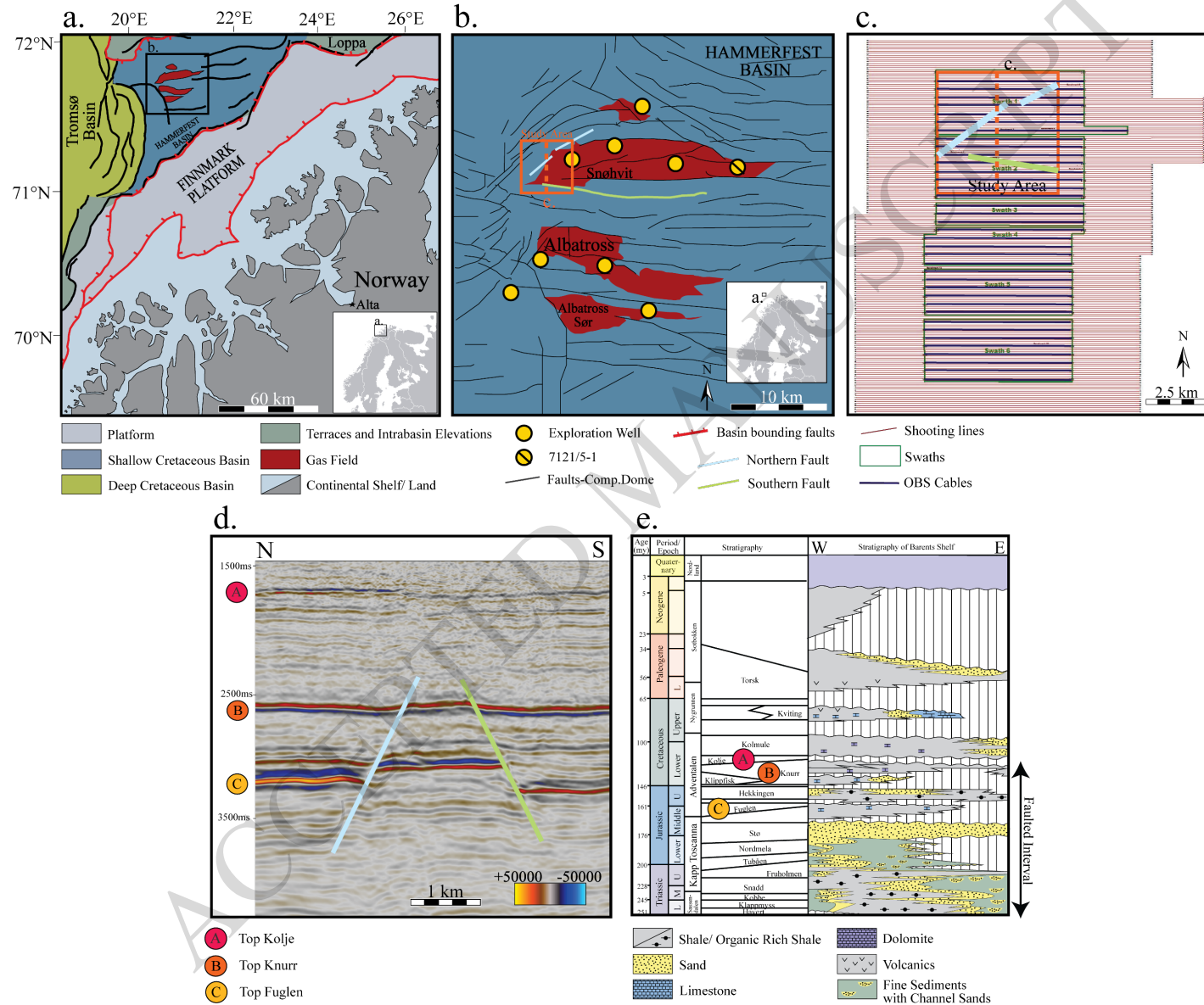


Figure 2

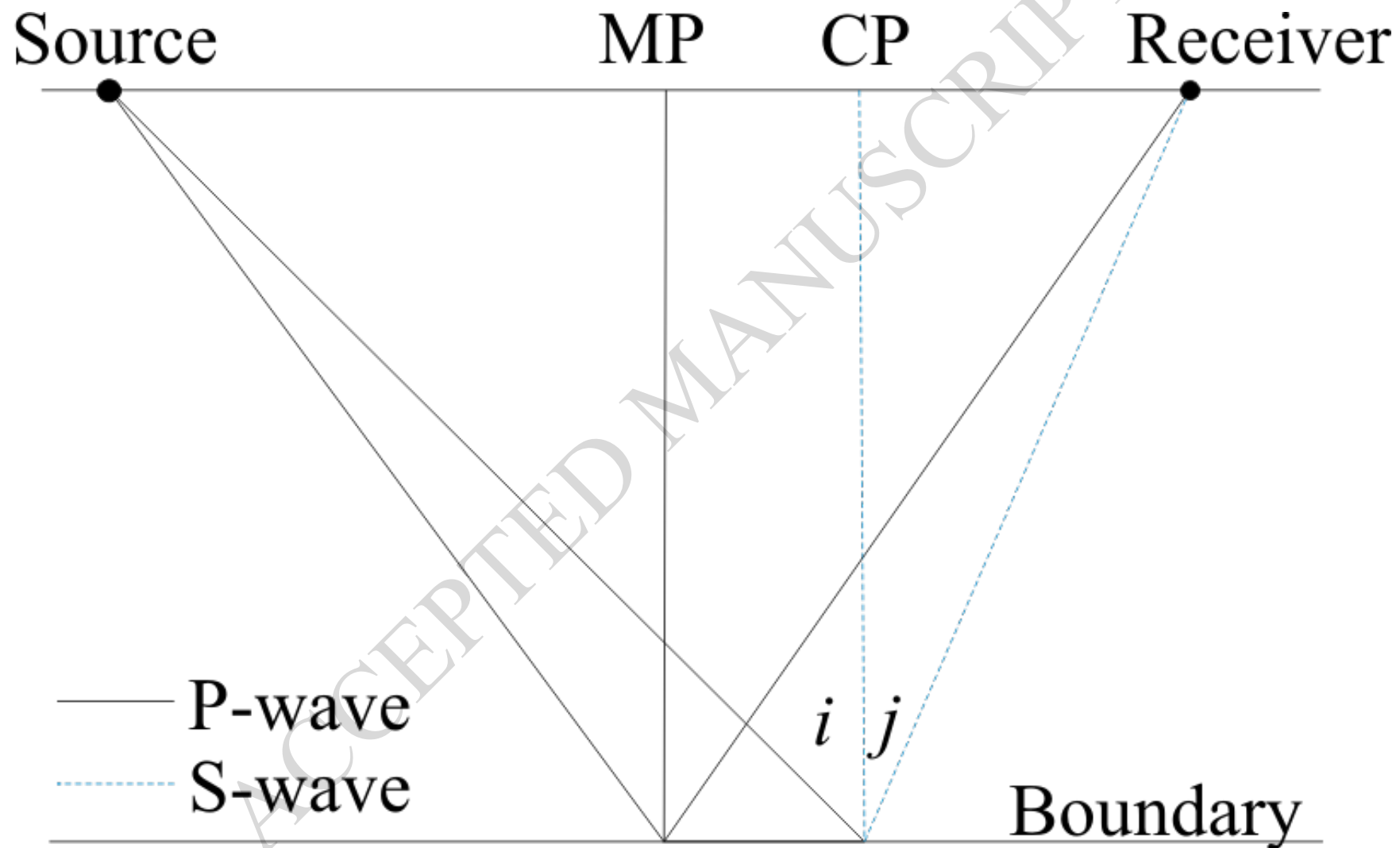


Figure 3

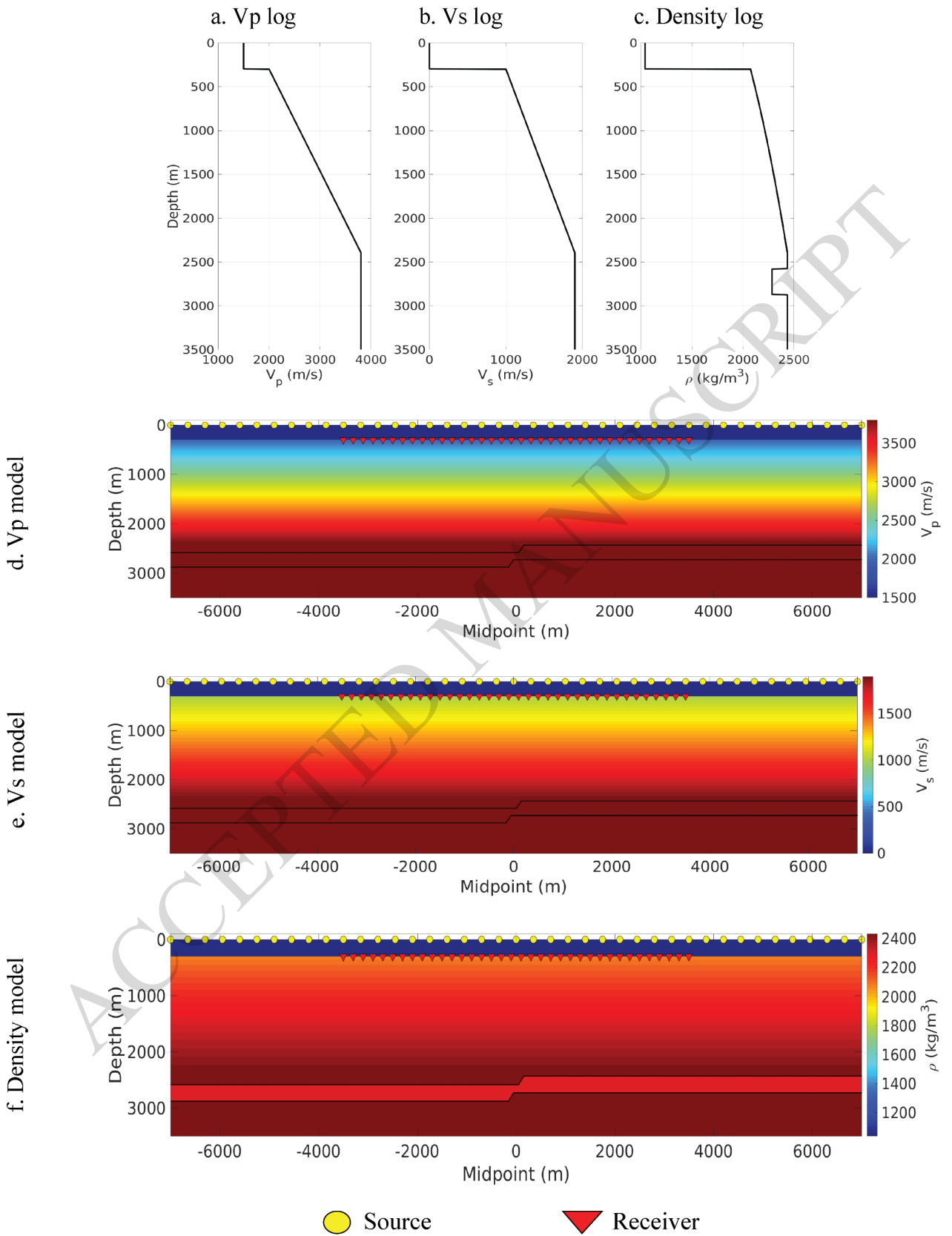


Figure 4

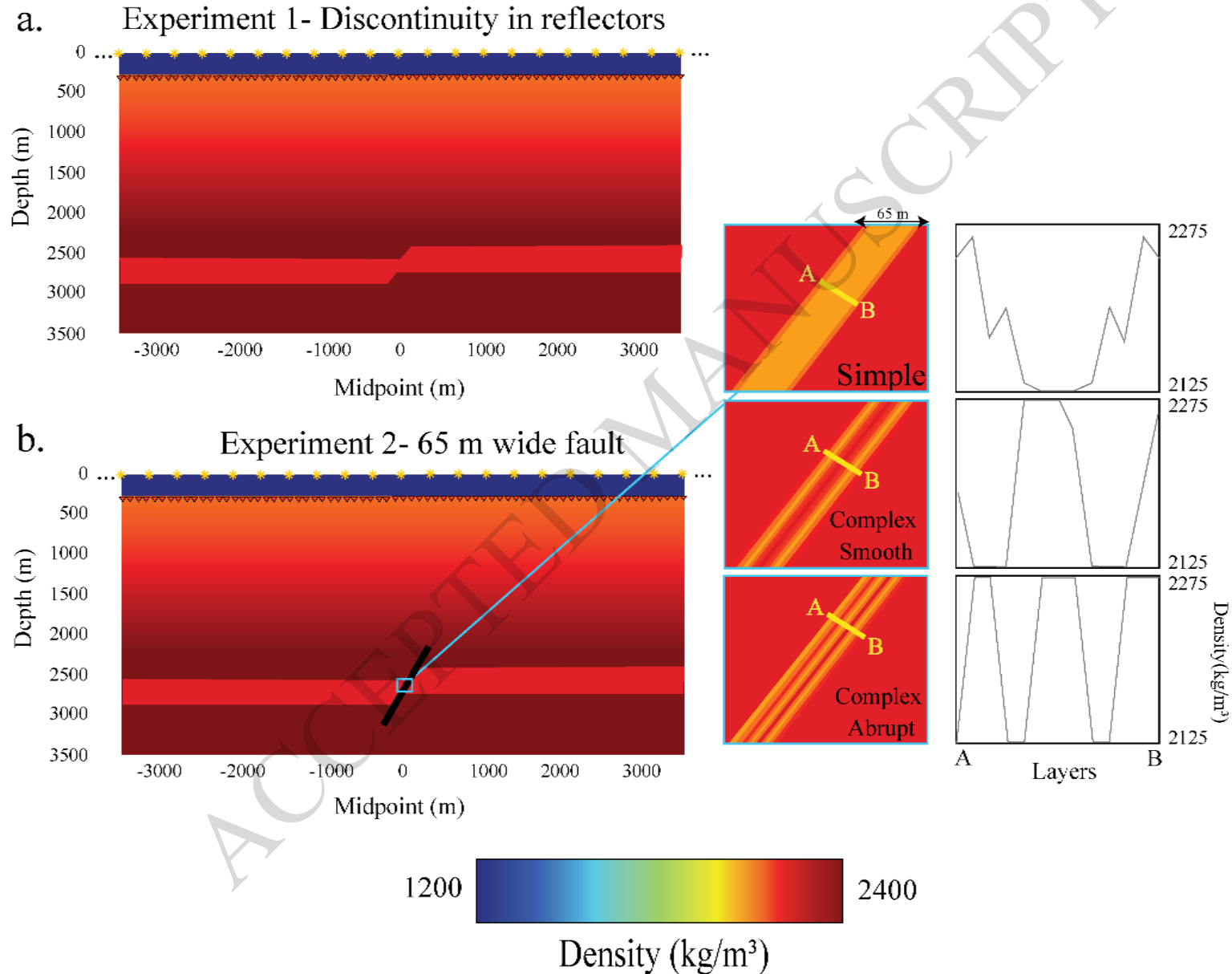


Figure 5

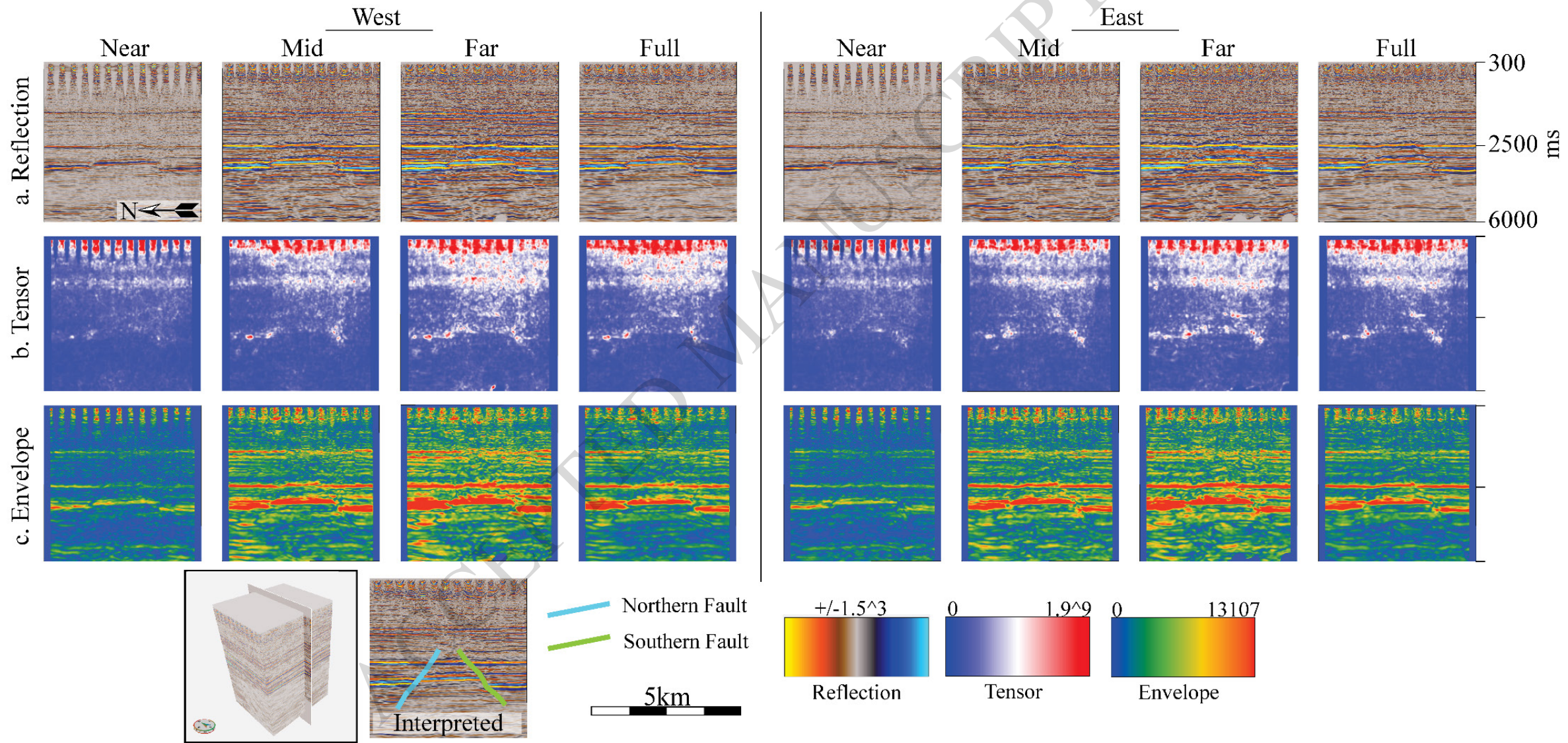


Figure 6

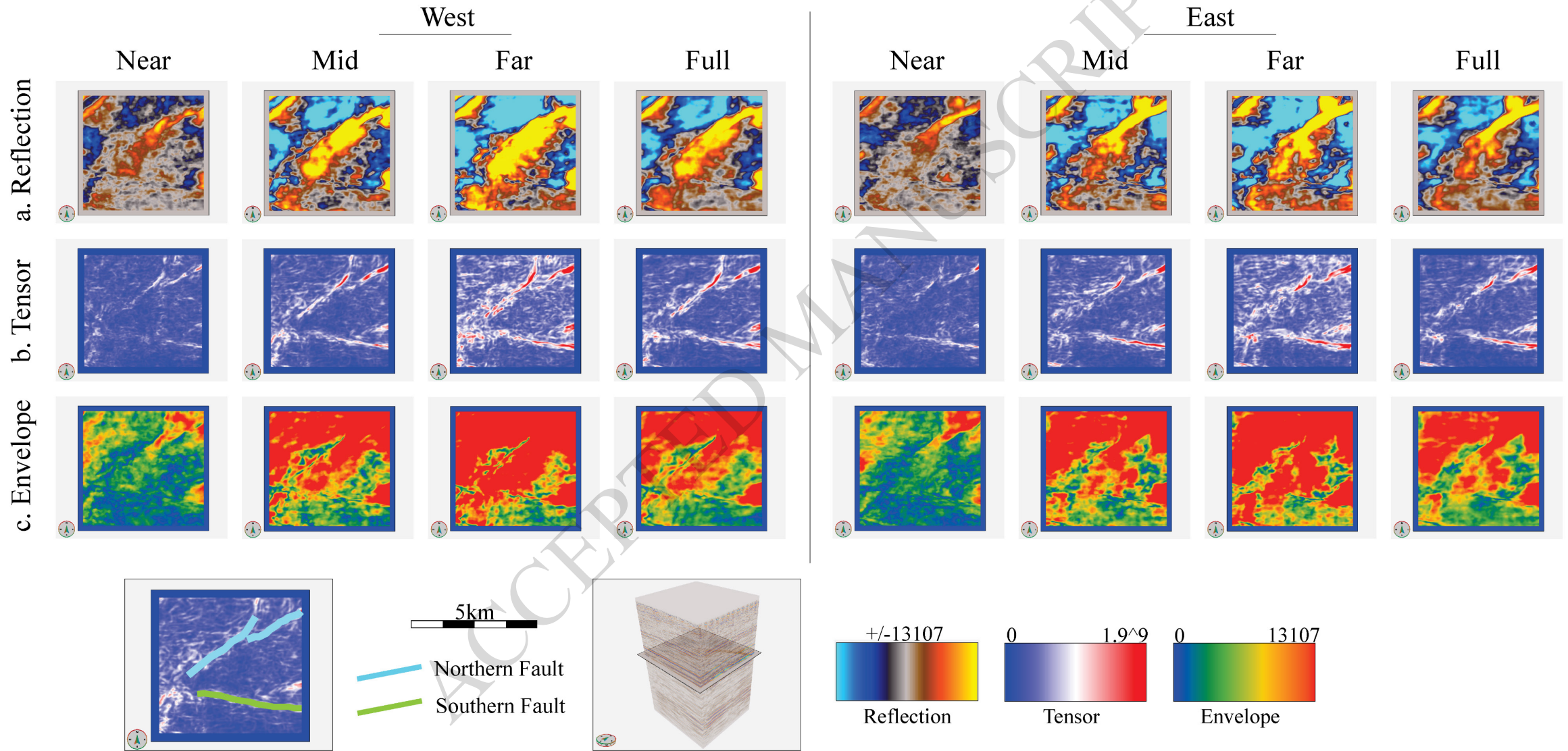


Figure 7

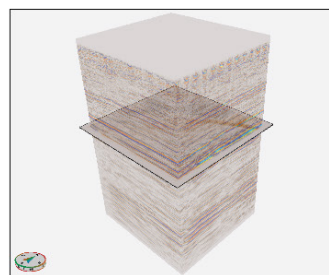
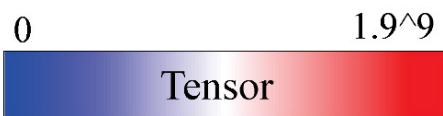
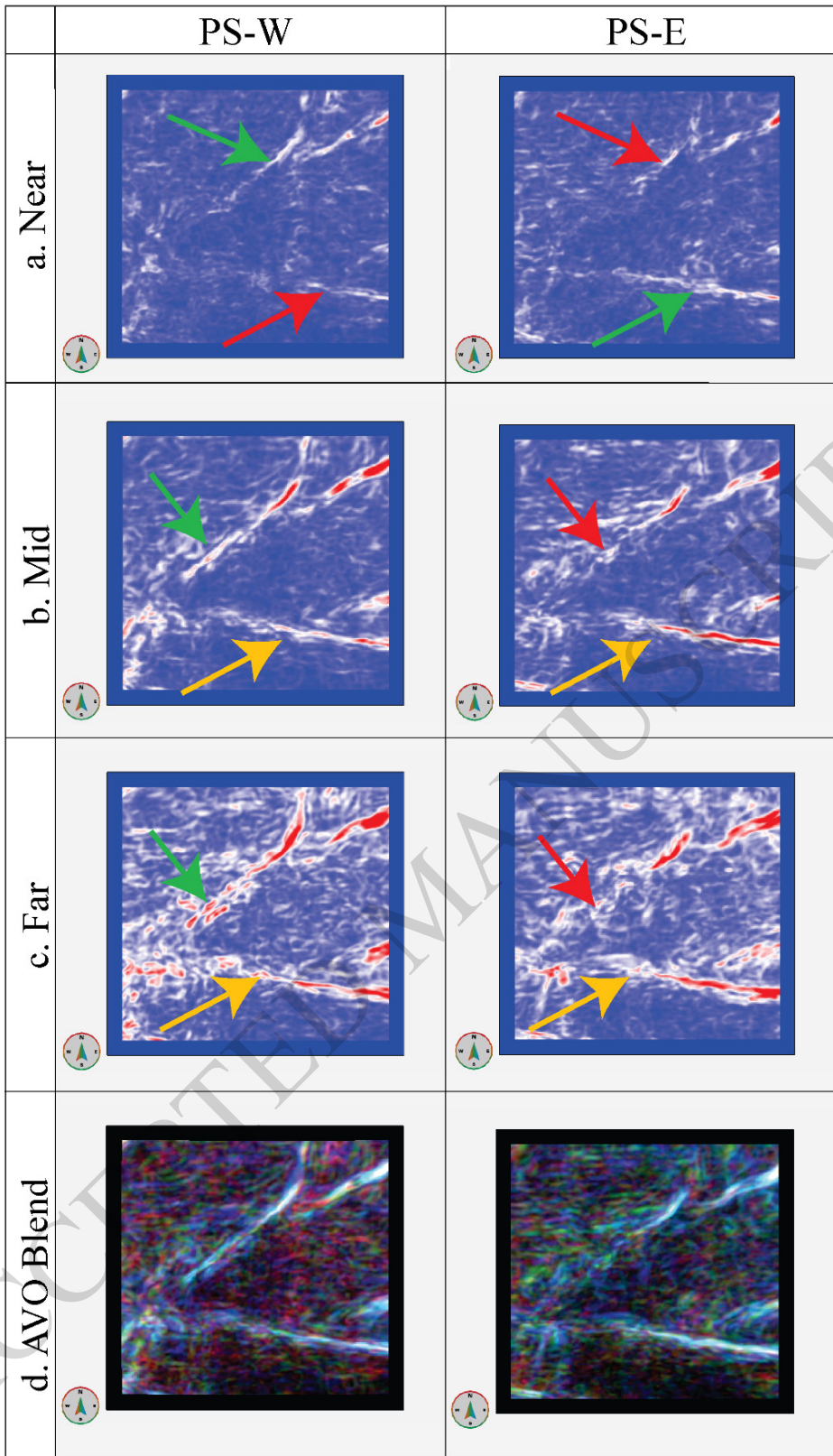


Figure 8

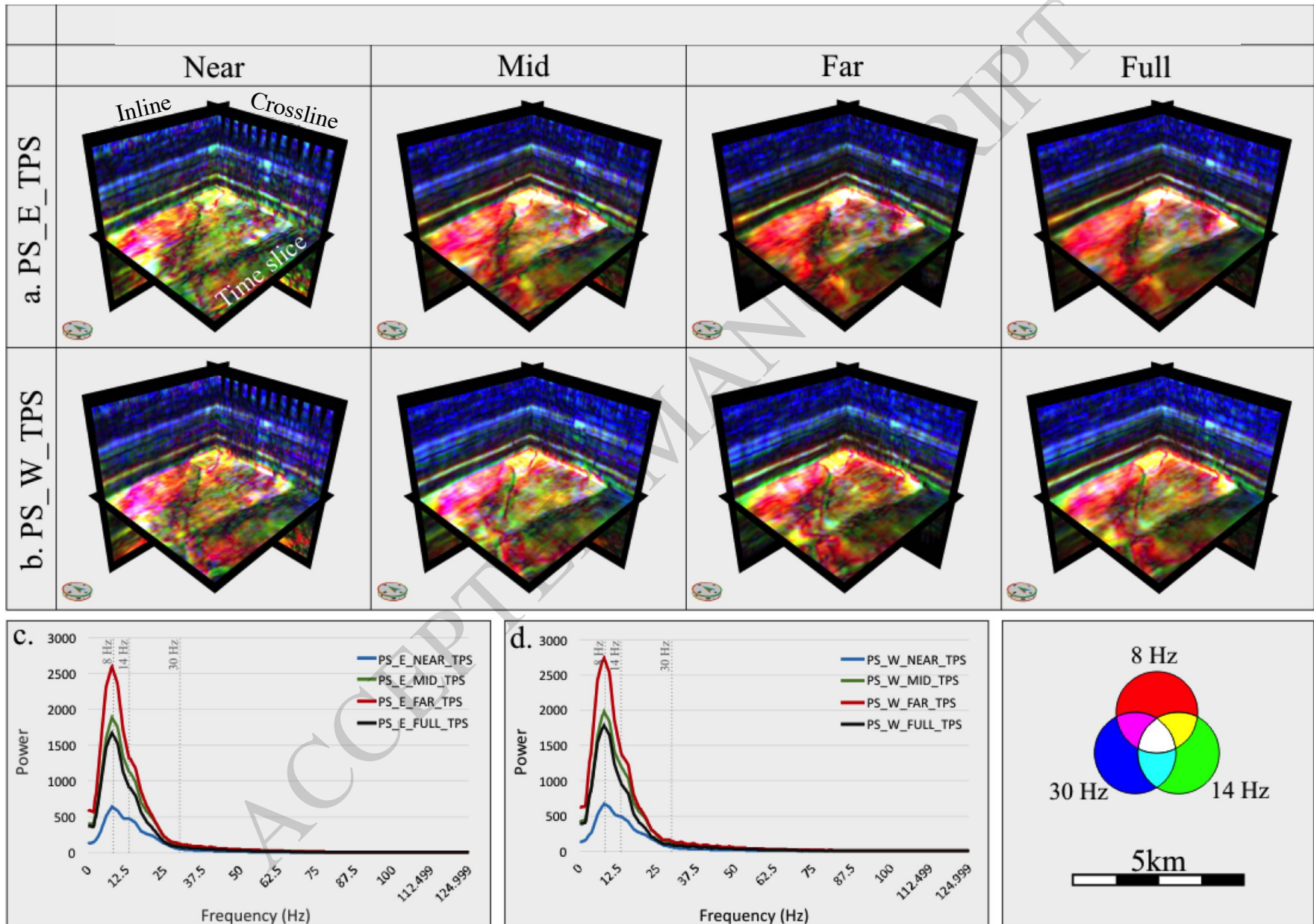


Figure 9

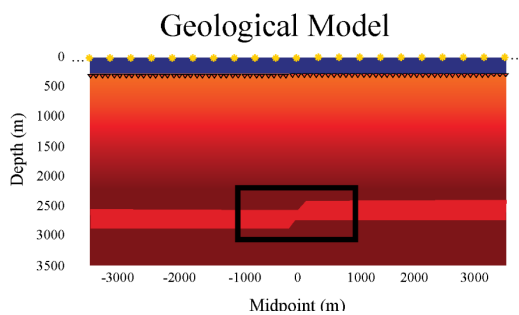
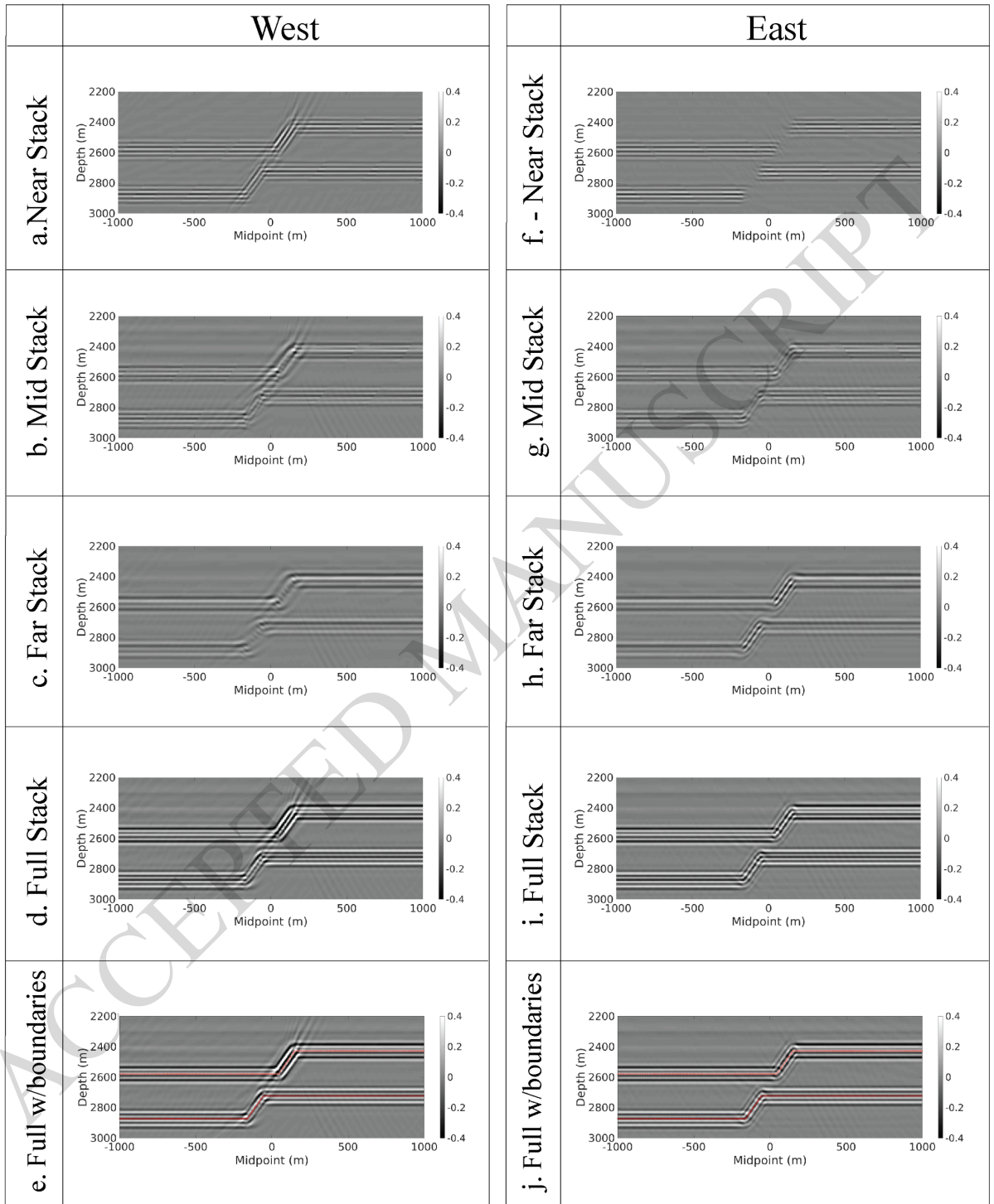


Figure 10

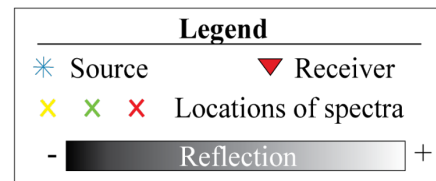
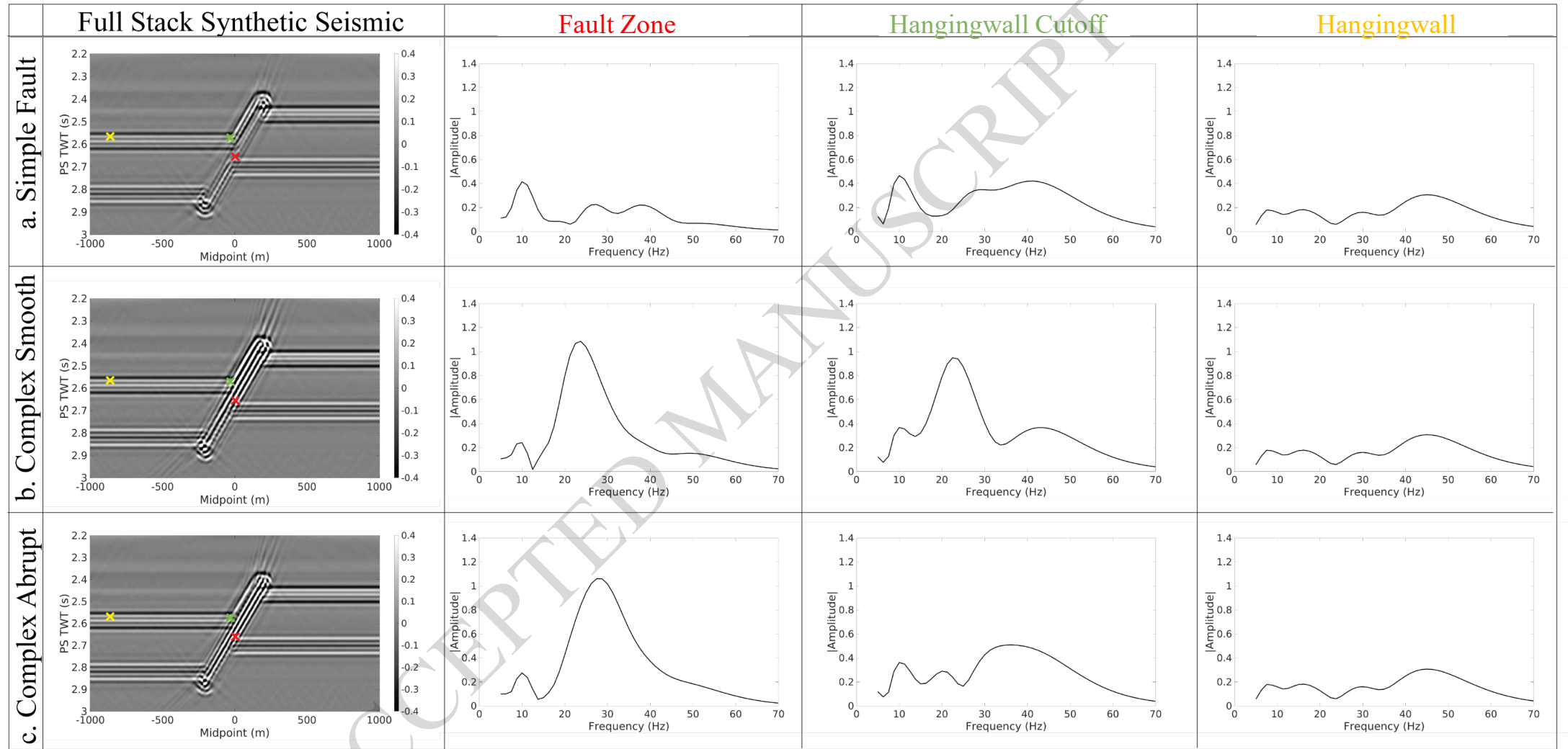
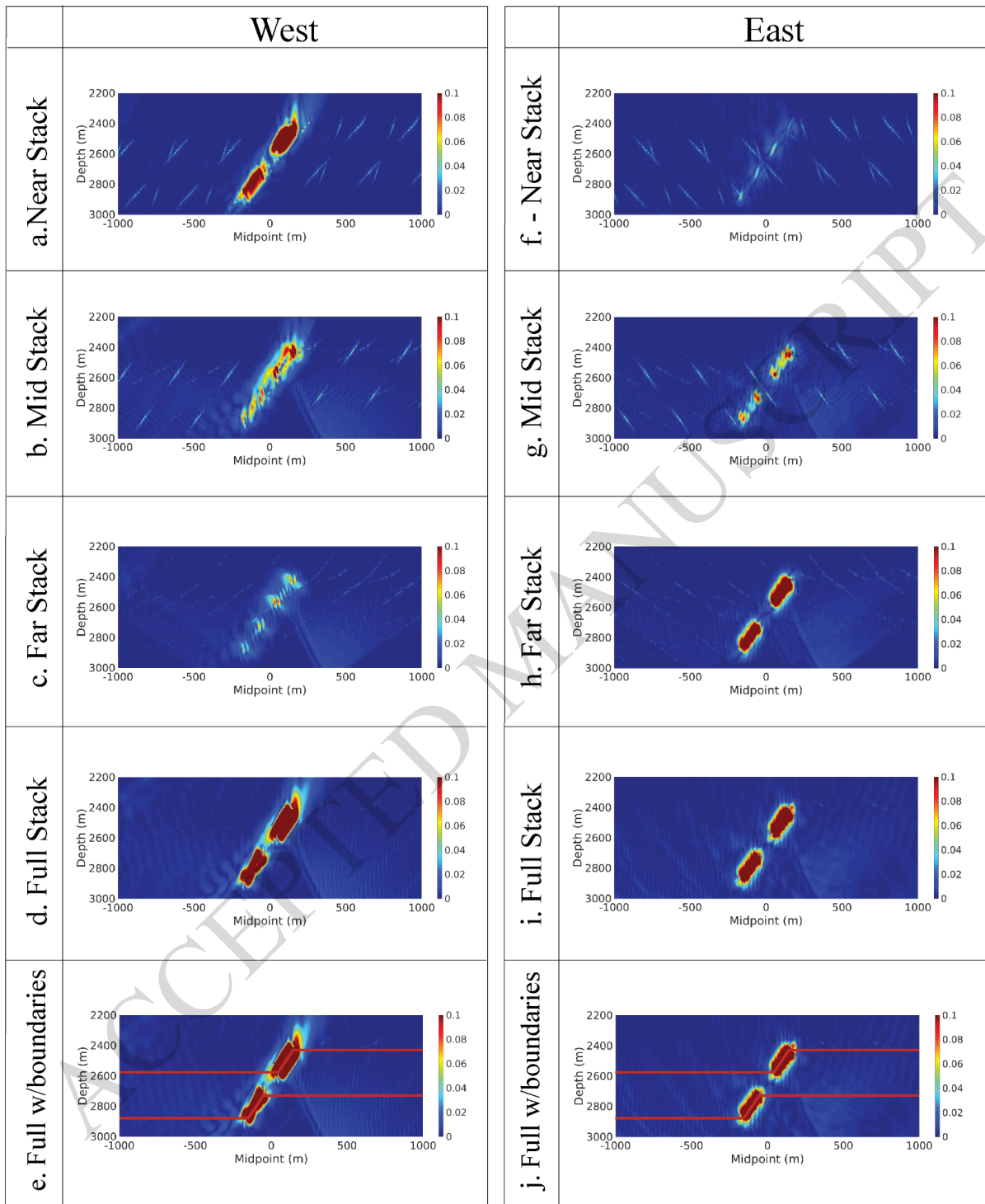


Figure 11



Geological Model

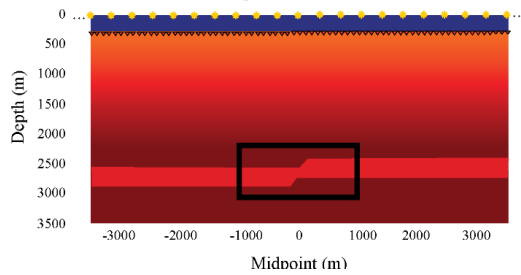


Figure 12

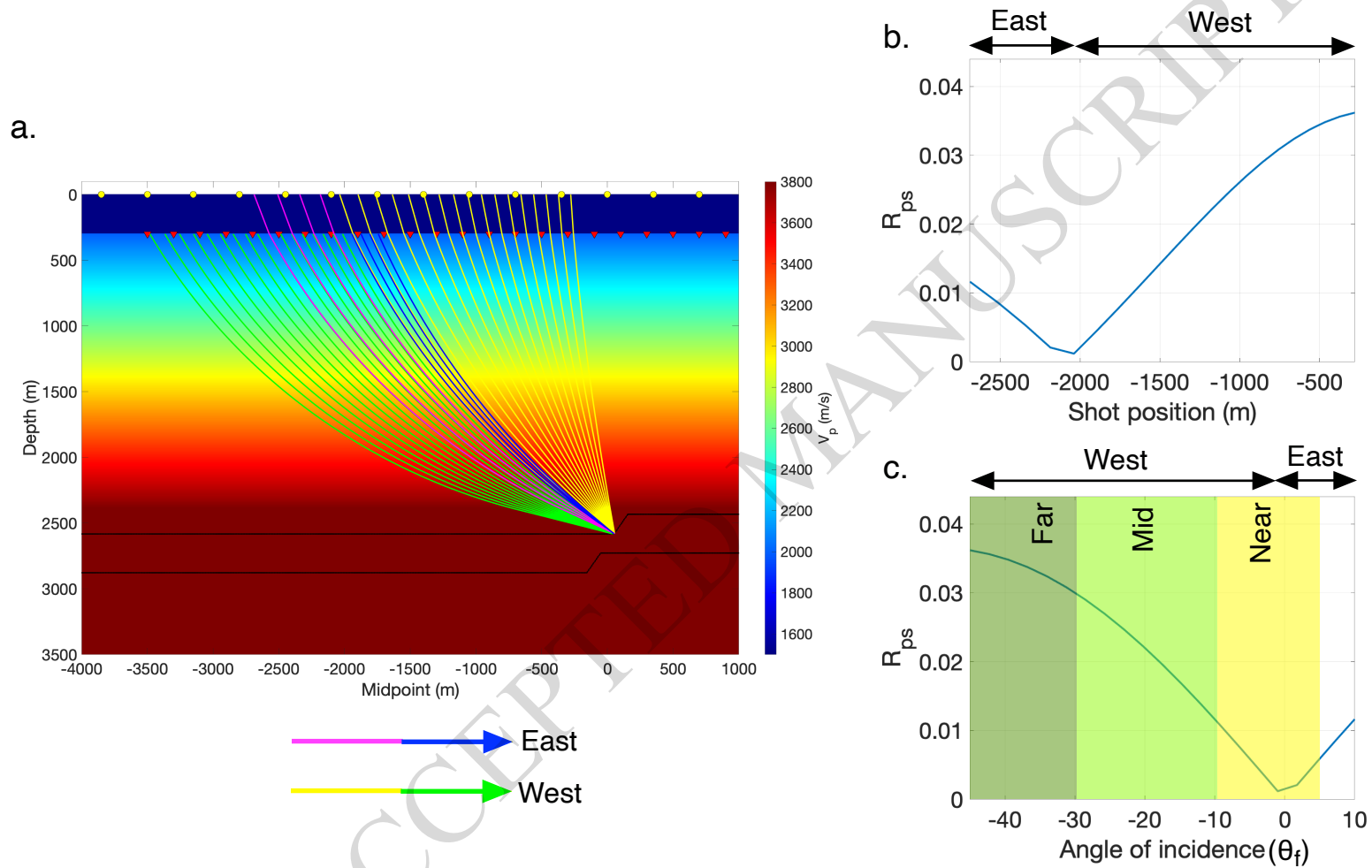


Table 1

Processing Workflow ST15M01	
Stage	Pre-processing
1	Reformat from SEG Y
2	Edits receivers
3	3 3C Reorientation
4	Anti alias filter, 94Hz 72dB/Oct
5	Resample from 2 to 4ms
6	Lowcut 3Hz 18dB/Oct
7	Impulsive noise attenuation
8	Tidal statics
9	Source depth statics
10	PZ sum cross-ghosting method with de-pegleg option
11	Vz noise attenuation
12	Zerophasing/Debubble/ refraction mute applied
13	2D shot interpolation 37.5 to 9.375m and 2D shotline interpolation from 25 to 12.5m
14	3D Tau-p mute and deconvolution
15	3D SRMM
16	Drop interpolated shotpoints
17	Diffracted multiple attenuation
18	Parabolic radon demultiple
19	Surface consistent amplitude corrections
20	TVF
21	Q-phase correction, where $Q = 130$, Freq. = 45Hz
22	5D regularization, offset/azimuth
23	3D Random noise attenuation
24	Separate azimuths 180-359 degrees (East) and azimuth 0-179 degrees (West)
25	PSDM Kirchhoff (using 1 iteration of TTI TOMOML velocity update)
Stage	Post Migration Processing
26	Stretch to time
27	Residual moveout corections
28	High resolution parabolic radon demultiple
29	3D Random noise attenuation
30	CDP trim statics
31	Angle mutes
Stage	Post Stack Processing
32	Full volume stack and angle stacks
33	Match ST9705Z14: Time shift =0.4msec Time variant amplitude scalars: 0.1 dB 0-900msec, 0.06dB 900-4800 msec
34	2D interpolation from 12.5x25 to 12.5x12.5 grid
35	Time variant gain, 3dB 0-3sec, 9dB at 4.8sec
36	Segy